All-optical Signal Processing Using Nonlinear Periodic Structures: A Study of Temporal Response

by

Winnie Ning Ye

A thesis submitted in conformity with the requirements
for the degree of Master of Applied Science
Graduate Department of Electrical and Computer Engineering
University of Toronto

Abstract

All-optical Signal Processing Using Nonlinear Periodic Structures: A Study of Temporal Response

Winnie Ning Ye

Master of Applied Science

Graduate Department of Electrical and Computer Engineering

University of Toronto

2002

This work presents the first time-domain analysis of pulse propagation through stable, balanced nonlinear periodic structures, with a focus on design towards all-optical signal processing applications. The propagation dynamics of ultrashort pulses in the nonlinear structures with varying grating lengths and linear grating strengths are investigated. In the absence of a linear grating, with two adjacent layers of nonlinear materials ($n_{1,2} = 1.50 \pm (2.5 \times 10^{-12}\ \mathrm{cm}^2/\mathrm{GW})I_{in}$), the pulse-bandwidth-dependent limiting behavior is investigated. The output peak intensity of a 600 fs input pulse is found to be limited to 1.2 GW/cm^2 for a 290 μm-long device. In the presence of a linear grating, S- and N-curve transfer characteristics are observed. A 720 μm-long device with a 0.01 out-of-phase linear grating (i.e., $n_{1,2} = (1.50 \mp 0.01) \pm (2.5 \times 10^{-12}\ \mathrm{cm}^2/\mathrm{GW})I_{in}$), compresses a pulse down to 12% of its original width. The results reported in this work point to the promise of such devices in signal processing.

Acknowledgements

I would like to express my sincere gratitude to my supervisor, Professor Ted Sargent, for his guidance and support throughout this project.

I would like also to take this opportunity to acknowledge Professor Dmitry Pelinovsky and Professor John Sipe for numerous insightful discussions, and encouragement throughout this project.

I am grateful to the members of Professor Sargent's group for their support and valuable friendship; in particular to Lukasz Brzozowski for his support, encouragement, and most importantly, sincere friendship during my most stressful time. It was a great pleasure to work with Lukasz for the past two years.

I am deeply indebted to Henry Wong and Thomas Szkopek, for their boundless encouragement, inspirations and great sense of humor. Special thanks are due to Aaron Zilkie, for his patience, support, and companionship.

I would like also to thank my parents, my sisters for their inspiration and encouragement throughout my life.

Finally, I acknowledge NSERC for the financial support during this work.

书山有路勤为径，学海无涯苦作舟!

Contents

List of Figures

Chapter 1

Motivation

Telecommunications networks now play an extremely important role in a world where global communication has become an essential element of everyday life. These networks demand great bandwidth for networking applications such as data browsing and massive file transfer on the Internet, multimedia-on-demand, video conferencing, and much more. To meet the increasing demand, economical and efficient technologies that provide higher capacity and improved networking are critical. Optical networking is the foremost of such technologies because it can offer higher speeds over long transmission distances, providing unbeatable cost-per-bandwidth due to the low loss and managed dispersion of optical fiber over a wide spectrum.

In principle, the maximum information capacity of a standard, commercially available optical fiber over 100 kilometers is around 3 b/s/Hz [1]. Coupled with a maximum fiber bandwidth of $\sim$ 50 THz (corresponding to a wavelength range from 1.2 to 1.6 μm), this means that an ultimate 150 Tb/s can be achieved. In practice, however, commercial networks are not capable of operating close to this rate. The transmission of multiple signals simultaneously over the same fiber provides a simple way for making use of the abundant information capacity offered by fiber optics [2]. In order to achieve the highest possible transmission rate, signal multipexing techniques – wavelength-division multiplexing (WDM) and time-division multiplexing (TDM) – are commonly employed. In March 2001, NEC Corporation set a new fiber optic transmission record of 10.9 Tb/s by transmitting 273 channels of data at 40 Gb/s per channel over 117 kilometers. However, the bit rate per channel is often limited to 40 Gb/s in commercial systems due to the speed of electronic components, and the optical limitations imposed by fiber dispersion and fiber nonlinearity. The two signal multiplexing techniques, WDM and TDM, are explained further in the next section.

1.1 WDM and TDM

WDM techniques involve transmitting multiple signals, each with different carrier wavelengths, simultaneously over a single optical fiber; while TDM techniques involve transmitting two or more signals over the same communications channel (on a given wavelength) by interleaving their bits in time. In other words, WDM provides a way to increase the transmission capacity by using multiple channels at different wavelengths and TDM provides a way to increase the effective bit rates on each channel. Thus TDM and WDM are two complementary approaches. The combination of TDM and WDM techniques can help in realizing point-to-point links that operate at ultrafast bit rates above 1 Tb/s [2].

However, in WDM networks, large numbers of closely spaced wavelengths give rise to interchannel crosstalk. This can lead to significant system degradation because of power transfer from one wavelength (channel) to the other. Furthermore, the nonlinearities associated with fiber – stimulated Raman scattering, four-wave mixing, and cross-phase modulation – limit the number of channels that can be transmitted simultaneously, and the spacing between these channels.

TDM, on the other hand, provides a very simple and effective way of subdividing a high-speed digital data stream into multiple slower data streams, which potentially improves the network performance in terms of user access time, delay and throughput. Commercially available TDM technology has achieved a transmission rate of 10 Gb/s with high-speed electronics. Functionally complex operations such as reshaping, retiming, and switching currently rely on electronics. The rate of such networks is constrained by the rate at which signals may be processed using electronic components. This rate-limiting effect is referred to as the *electronic bottleneck*.

A necessary first step in advancing TDM beyond the rate of electronics is to multiplex multiple time-domain streams via *optical time division multiplexing* (OTDM). Special considerations for the capability of handling the ultrafast optical signals are required in implementing an OTDM network. The functional units that constitute an OTDM network include devices for the generation of optical pulses, multiplexing, transmitting, demultiplexing, and signal processing [3].

Optical sources such as mode-locked semiconductor lasers and mode-locked fiber lasers are capable of generating narrow optical pulses with high repetition rates. Multiplexing can be implemented by splitting the modulated optical pulse train into multiple streams and subsequently combining them after subjecting these streams to progressively increased fiber delays. In contrast to the passive multiplexing operation, the demultiplexing operation requires fast optical AND gates to estimate accurately the clock timing of the incoming signal. Nonlinear optical loop mirrors (NOLMs) are available for this purpose. Solitons are attractive for optical communications because they are able to maintain their width and shape in spite of fiber dispersion effects. However, their use requires substantial changes in system design (e.g., so as to generate and maintain their high peak power during the course of propagation [3]) compared with non-solitonic systems. Ultrafast signal processing functions including switching, logic gate operations, and pulse reshaping (in non-solitonic systems only) are in general required for ultrashort pulse propagation in OTDM networks.

To date, practical all-optical processing devices such as optical logic gates and optical pulse reshapers are still not commercially available. As a result, commercialized OTDM systems are yet to be realized. Intense research has been engaged on efficient and practical signal processing devices. Devices such as nonlinear directional couplers, nonlinear Mach-Zehnder interferometers, nonlinear optical loop mirrors, nonlinear Fabry-Perot resonators, and nonlinear periodic structures have been theoretically predicted to perform time-domain signal switching, regeneration, reshaping, and logic functions entirely in the optical domain. [3] Thus, it is necessary to study the temporal behavior of the potential signal processing devices in order to evaluate their suitability for use in all-optical networks.

Before getting into the details of the design of a specific device, a brief introduction of the mentioned signal processing devices is required. The following section describes these time-domain processing devices, summarizes their functionalities, and introduces the device considered in this thesis.

1.2 Nonlinear Time-domain Signal Processing Devices

1.2.1 Mach-Zehnder Interferometer

A nonlinear Mach-Zehnder interferometer has a nonlinear element on one of the two parallel arms, as illustrated in Figure 1.1 [4]. In the nonlinear element, the properties of

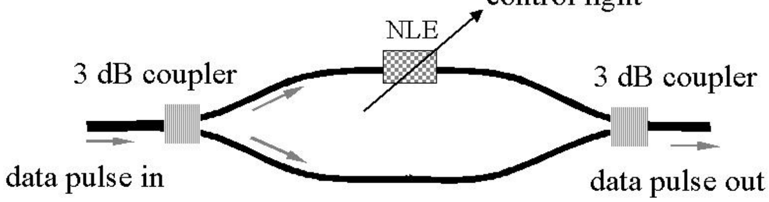

Figure 1.1: A nonlinear Mach-Zehnder Interferometer (MZ).

the medium are dependent on the intensity of the supplied optical field. In other words, the presence of an optical field modifies the properties of the medium, which in turn, modifies another optical field or the original field itself. The refractive index (n) of a nonlinear material can be expressed as:

$$n = n_0 + n_2 I, \tag{1.1}$$

where n_0 is the linear part of the refractive index, and n_2 is the Kerr coefficient of the material. In the case of the Mach-Zehnder interferometer, the control signal modifies the data signal by altering the phase shift experienced by the signal traveling in the nonlinear arm. In the absence of the control signal, the low-power data signal is split into the two arms at the input and is recombined at the output port where the two optical fields interfere constructively. Thus the input pulse is reproduced at the output. If a control signal is present such that a π relative phase shift is introduced between the two arms, the optical fields recombine at the output port and interfere destructively. The result is no output. A Mach-Zehnder interferometer can therefore act to switch signals on and off depending on the the control signal. This is in effect a logic NAND operation. If two control signals are introduced, one for each nonlinear arm, the Mach-Zehnder interferometer can behave as a two-input XOR gate.

1.2.2 Fabry-Perot Resonator

A Fabry-Perot resonator consists of two parallel, highly reflective mirrors separated by a distance d. In a nonlinear Fabry-Perot device, the medium in between the mirrors is optically nonlinear, as shown in Figure 1.2(a). The input-output relation for this system (Figure 1.2(b)) forms a hysteresis loop, making this device a bistable system. By definition, a bistable system has an output that can take only one of two distinct stable values [4]. Switching between these values may be achieved by a temporary change of the level of the input. At a low input power (point a), the nonlinear effect is negligible,

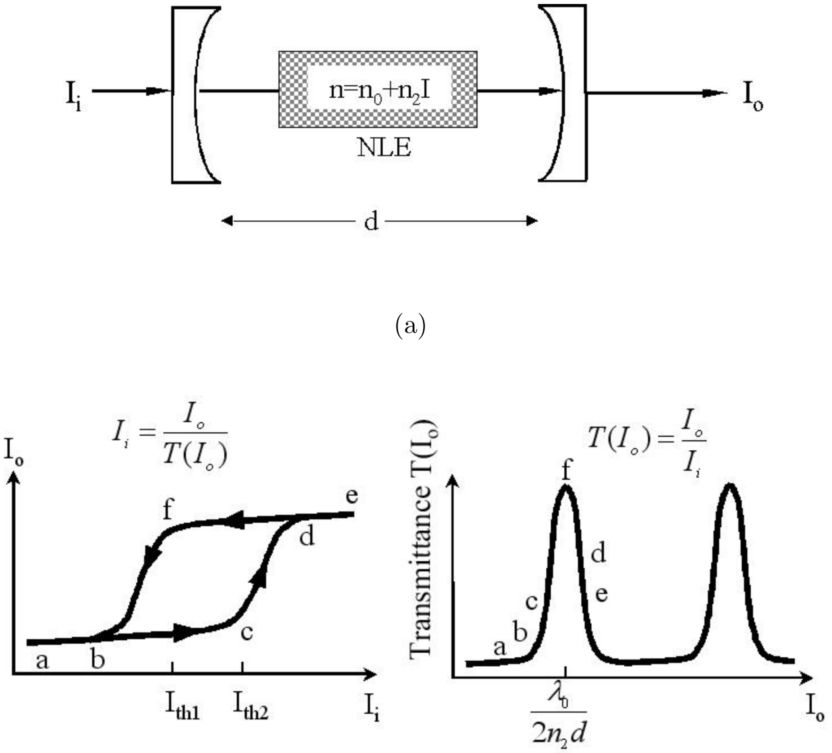

(a)

(b)

Figure 1.2: (a) A nonlinear Fabry-Perot resonator. (b) Input-output relation: a bistable system (reproduced from [5]).

resulting in low transmission. As the input power is increased, the power accumulates in the resonator, but the transmission remains relatively low, until point *c* (threshold intensity I_{th2}) is reached. Further increase of the input power switches the device to a high-transmission state (point *d*) because the device operates near the resonance. At a higher input power (point *e*), the device is tuned away from the resonance, therefore reducing the power in it. As the input power is decreased, the device will remain in the high-transmission state until point *f* (threshold intensity I_{th1}) is reached. For a lower input power, the device will switch to the low-transmission state (point *b*) because the device is further away from the resonance. This process is described in detail by Smith *et al.* [5]. The system therefore takes its low value for small inputs ($I_i < I_{th1}$) and its high value for large inputs ($I_i > I_{th2}$), where I_{th1} and I_{th2} are the thresholds as shown in Figure 1.2(b). In the intermediate range, $I_{th1} < I_{in} < I_{th2}$, however, any slight change forces the output to either the upper or lower branch depending on the initial state. Thus, such a bistable device can function as a switch, a logic gate, and a memory element.

1.2.3 Directional Coupler

When two waveguides are sufficiently close, light can be coupled from one waveguide to the other. A nonlinear direction coupler works based on this principle (Figure 1.3 [4]). The refractive indices and the dimensions of the waveguides may be selected so that when the input optical power is low, it is channeled into the other waveguide; when it is high the refractive indices are altered in the nonlinear material and the power remains in the same waveguide [4]. The detuning induced by the Kerr nonlinearity effectively switches the input signal from one waveguide to the other. Besides switching and performing logic operations, the device can be also used to sort a sequence of weak and strong pulses, separating them into the the two output ports of the coupler, as illustrated in Figure 1.3.

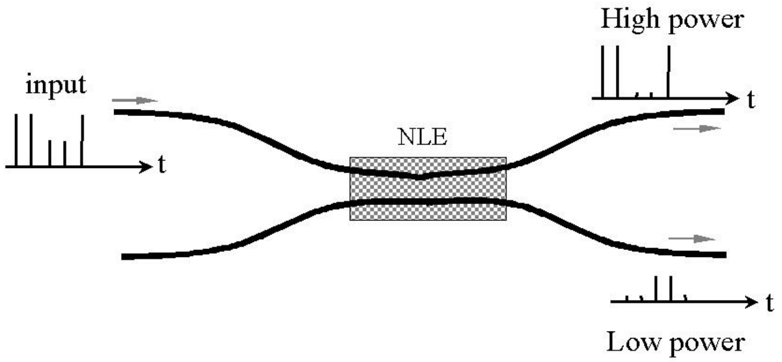

Figure 1.3: A nonlinear directional coupler (sorting a sequence of weak and strong pulses).

1.2.4 Optical Loop Mirror

A nonlinear optical loop mirror (NOLM) is constructed by using a fiber loop whose ends are connected to the two input ports (A and B) of a 3-dB coupler [2], as illustrated in Figure 1.4(a). In the absence of a control pulse, the NOLM reflects its input entirely to port A because the two counter-propagating waves in the fiber loop experience the same phase shift over one round trip. However, if a strong control signal is coupled into the loop to meet with only one pulse, a refractive index change is induced in the nonlinear fiber. The path length of the loop is chosen such that a phase shift of π happens between the two counter-propagating signals in the presence of a strong control pulse. The π phase shift creates a complete switch – an output pulse emerges from the port B.

By introducing a nonlinear element (NLE) asymmetrically to the fiber loop, the configuration becomes a *terahertz optical asymmetric demultiplexer* (TOAD). The advantage of this configuration over NOLM is that the length of the fiber loop can be much shorter since the added NLE has a higher nonlinearity than the silica fiber. Figure 1.4(b) shows the details of a TOAD. The control pulse needs to possess sufficiently high power so that the optical properties of the NLE can be significantly altered. This in turn can change the phase shift undergone by the pulse propagating in the fiber loop. For proper operation of the TOAD as a demultiplexer, the timing between the control and signal pulses is critical. If the control pulse arrives at the NLE between the two signal pulses, the signal pulses will emerge from port B when they have a π phase difference, otherwise the pulses will emerge from port A. Due to the asymmetry of the NLE, the TOAD can act as a logic gate to perform an AND function with the input signal from port A and the control signal. Both NOLMs and TOADs can perform switching and logic operations.

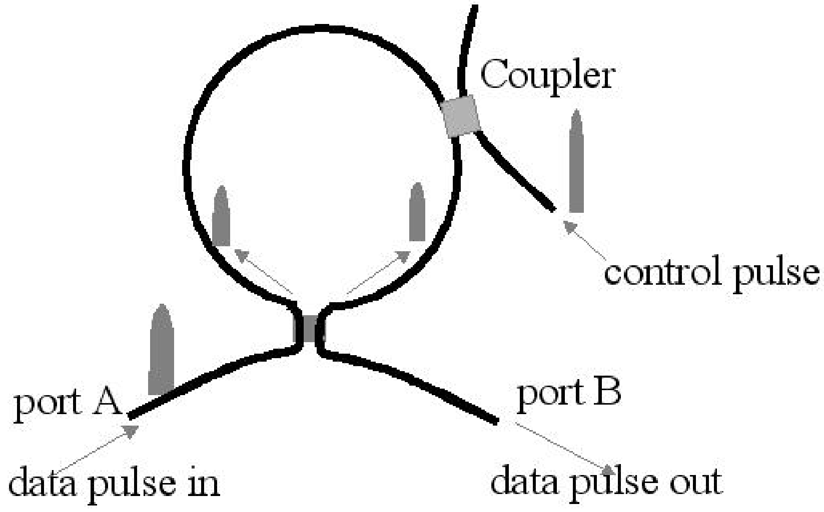

(a)

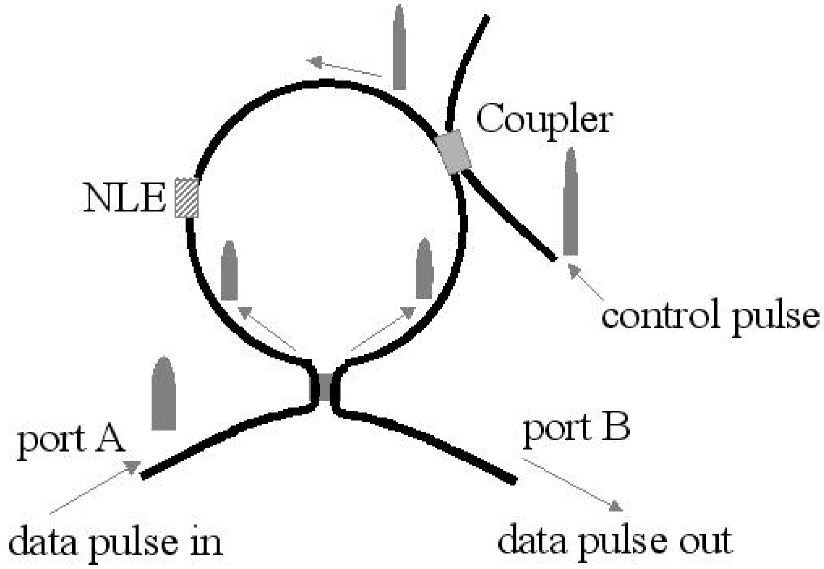

(b)

Figure 1.4: (a) A nonlinear optical loop mirror (NOLM). (b) A terahertz optical asymmetric demultiplexer. (Reproduced from [3].)

1.2.5 Periodic Structure

A simple nonlinear periodic structure consists of alternating layers of linear and nonlinear materials, as shown in Figure 1.5. As a light beam propagates through a nonlinear periodic structure, it experiences multiple reflections upon successive periods inside the structure. By adjusting the period and the index of the materials, constructive interference in reflection can occur such that the light with one wavelength can be reflected completely and the other wavelengths are still transmitted. Light of frequencies lying within the stopband evanesce in this manner.

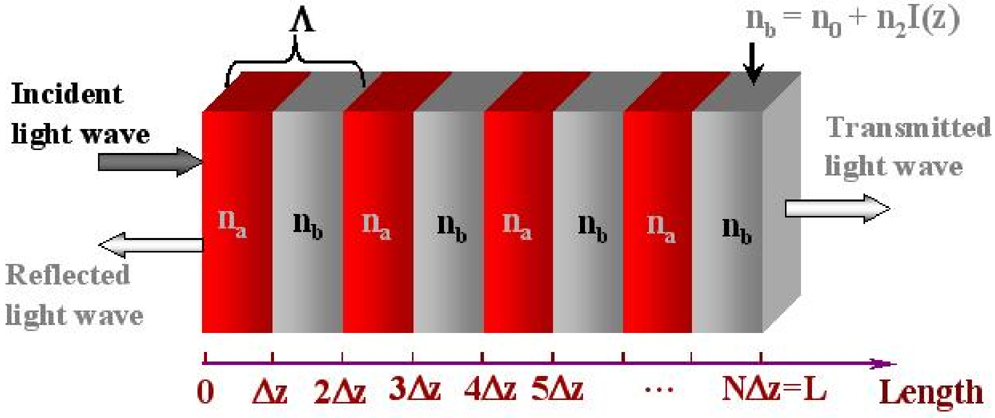

Figure 1.5: Schematic of a simple nonlinear periodic structure with periodicity Λ. The two adjacent layers consist of one linear material with refractive index n_a and one nonlinear material with intensity-dependent refractive index $n_b(I)$.

In a nonlinear periodic device, the spectral position as well as the strength of the stopband may in general be intensity-dependent. The dynamic shift of the stopband can detune a frequency component out from the Bragg condition at high intensities, thus allowing the frequency component to propagate through the system unimpeded – realizing the switching function. Besides switching, periodic nonlinear structures have also been either theoretically predicted or experimentally demonstrated to give rise to pulse compression [6, 7], limiting [8, 9, 10, 11, 12], and logic operations [13, 14]. These potential abilities in self-processing of temporal pulses motivate research into exploring novel designs of nonlinear periodic structures to search for new functionalities and to evaluate their prospective performance.

1.3 Thesis Focus

This thesis considers a specific class of nonlinear periodic structures, investigates and evaluates their potential signal processing abilities, and discusses their practicality. An understanding of the fundamental concepts and previous research are presented in Chapter 2. In order to explore the time-domain signal processing capabilities of the device, theoretical and numerical algorithms are used to simulate the device performance in the time domain. Chapter 3 describes the analytical framework of the numerical algorithms, and Chapter 4 describes the details of the simulation model for simulating the device performance. Chapter 5 investigates the temporal behavior of the device, demonstrating the limiting and pulse reshaping signal processing abilities.

Chapter 2

Literature Review and Thesis Objective

2.1 Introduction

It was explained in the preceding chapter that nonlinear periodic structures have multiple potential applications in all-optical signal processing. In this chapter, a detailed survey of the literature on the subject of nonlinear Bragg gratings is presented. It begins with a brief summary of some basic concepts of Bragg gratings and nonlinearity and a list of new capacities which can be created by combining the two. Then follows a survey on past research on nonlinear Bragg gratings. The concepts of both solitonic and non-solitonic pulse propagation in these Bragg gratings are discussed. Based on this review, the objective of the thesis is formulated and the remainder of this work is laid out.

The present chapter reviews previous findings on nonlinear Bragg gratings. The chapter lays a foundation for the remainder of the thesis by identifying what is known and what is missing in nonlinear periodic device operations. It proposes an avenue in order to fill the gap identified in the published literature.

2.2 Background on Nonlinear Bragg Gratings

Before discussing the complexities of nonlinear Bragg gratings, this section reviews some basic concepts of Bragg gratings and nonlinearity.

2.2.1 Linear Bragg Gratings

Bragg gratings have attracted much attention in the linear regime for many years. In its simplest form a Bragg grating consists of a periodic modulation of the refractive index, as illustrated in Figure 2.1. By properly designing the periodic layered medium, it can achieve extremely high reflectance for a selected spectral region, hence acting as a reflector for an incident monochromatic plane wave in this spectral region. In the case of a periodic medium made of layers of two materials with different linear refractive indices, constructive interference in reflection occurs when the resonance condition, called the *Bragg condition*, is satisfied:

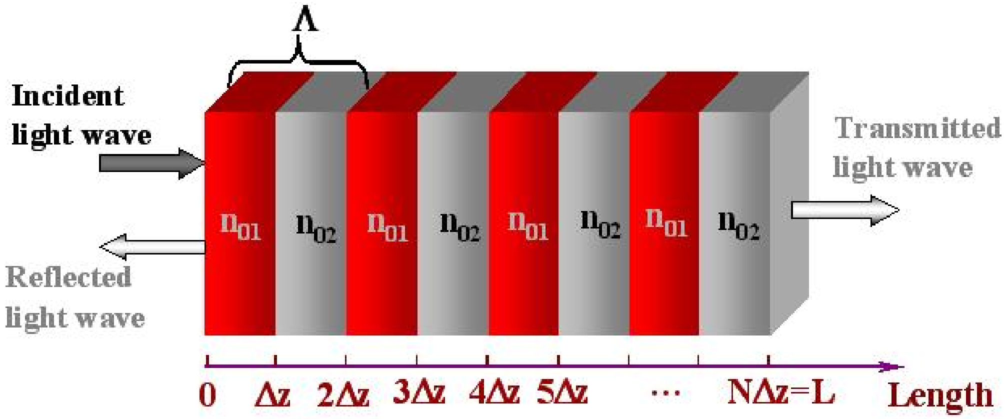

Figure 2.1: Schematic of a linear Bragg grating with periodicity Λ: n_{01} and n_{02} are the linear refractive indices of two adjacent layers.

$$\lambda_0 = 2\bar{n}\Lambda. \tag{2.1}$$

Here Λ is the period of the grating, $\bar{n}$ is the average refractive index, and λ_0 is the wavelength of the light impinging on the periodic structure. At a wavelength far from this Bragg condition, the light that is reflected upon the successive periods of the structure is out of phase. As a result, the light that propagates through the structure is essentially unimpeded, allowing the incident wave to transmit through without much reflection. However, if the frequency of the incident wave is within the so-called stopband range, the wave becomes evanescent. This phenomenon is referred to as *Bragg resonance*. The bandwidth of the stopband of a periodic medium is given by [15]:

$$\Delta\lambda_{gap} \cong \frac{2}{\pi}\frac{\Delta n}{\bar{n}}\lambda_0, \tag{2.2}$$

where Δn is the index difference between the adjacent alternating materials. It can be seen that the bandwidth of the device can be tuned by adjusting the refractive indices of the adjacent layers.

The wavelength-selective nature of Bragg gratings allows for linear, wavelength-domain optical signal processing applications in optical communications [14], including wavelength filtering and dispersion compensation. Various types of fiber Bragg gratings (FBGs) have also been commercially applied in optical fiber sensor systems [9, 14].

2.2.2 Nonlinearities in Optical Materials

The field of nonlinear optics explores and exploits the modification of the optical properties of a material system in the presence of light [16]. The invention of the laser in 1960 enabled examinations of the behavior of light in optical materials at higher intensities, making the study of nonlinear optics possible. To the existing advantages of linear optics, nonlinear optics can add further improvements and efficiency to switching and routing by manipulating light with other light that controls the properties of the medium. Thus, ultrafast nonlinear devices can contribute to alleviating the electronic bottleneck by implementing critical signal processing operations without the need to convert into the electronic domain.

The concept of the Kerr nonlinearity was briefly introduced in the last chapter (see Section 1.2.1). The intensity-dependent refractive index of a nonlinear material is defined in Eq. (1.1). An optical wave traveling in a Kerr nonlinear medium undergoes *self-phase modulation* (SPM). The phase shift experienced by a pulse of intensity $I(z,t)$ traveling over a distance Δz due to SPM is given by: $\Delta\phi_{SPM} = \frac{\omega}{c}\Delta z n_2 I(z,t)$. The dependence of the phase shift on frequency leads to chirping (i.e., the distribution of the pulse's instantaneous frequencies vary temporally). The intensity dependence of the refractive index in Eq. (1.1) can also lead to another nonlinear phenomenon, known as *cross-phase modulation* (XPM). Unlike SPM where a pulse induces a phase shift by its own intensity, XPM occurs when two or more signals interact with each other. Thus, the total phase shift for a specific signal wave depends on both the intensity of the signal wave and the intensity of other simultaneously transmitted signal waves. The phase shift for the jth signal wave over a distance Δz with M signal waves in a medium due to both SPM and XPM is $\Delta\phi_j^{NL} = \Delta\phi_{(j)SPM} + \Delta\phi_{(j)XPM} = \frac{\omega}{c}\Delta z\left(n_2 I_j + 2\sum_{m\neq j}^{M} n_2 I_m\right)$ [2].

Group velocity dispersion (GVD) must be considered in any analysis of nonlinear interactions since it determines the path length over which nonlinearly-interacting pulses influence one another. It is also significant in ultrashort pulse propagation systems because optical pulses have relatively large spectral bandwidth. Different spectral components of a pulse travel at different group velocities, causing the pulse to change its temporal width as it propagates. For short optical pulses the dispersive and nonlinear effects act together on the pulse and lead to new features. In particular, a pulse can maintain its temporal shape and travels indefinitely through a nonlinear medium when the SPM and GVD effects compensate each other completely. This is known as a soliton which will be discussed later in this chapter.

2.2.3 Nonlinearity with Periodicity

The previous two sections introduced the fundamental concepts and potential applications of Bragg gratings and nonlinearity. In this section we ask: "what if nonlinearity and periodicity are combined?"

Figure 1.5 illustrates a simple nonlinear periodic structure which consists of alternating layers of linear and nonlinear materials. Adding nonlinearity to the considerations of the stopband in a Bragg structure, the Bragg frequency in Eq. (2.1) and the bandwidth of the stopband in Eq. (2.2) can be rewritten by replacing the refractive indices with intensity-dependent ones:

$$\omega_0 = \frac{\pi c}{\bar{n}(I)\Lambda}, \quad \Delta\omega_{gap} \cong \frac{2}{\pi}\frac{\Delta n(I)}{\bar{n}(I)}. \tag{2.3}$$

The above equations suggest that both the size (width and depth) of the stopband $\Delta\omega_{gap}$ and the position of the center frequency ω_0 may potentially change with incident intensity. Therefore, the transmission of light through a nonlinear periodic stack is both wavelength- and intensity- dependent, as illustrated in Figure 2.2. The Kerr coefficient is assumed to be positive in this case. According to Eq. (2.3), and demonstrated with the three curves in Figure 2.2, the Bragg resonance frequency ω_0 shifts to lower frequencies with increasing intensity; while the width of the stopband widens with increasing intensity.

The above description of the dynamic movement of the stopband with intensity shows nonlinear Bragg structures as excellent candidates for all-optical signal processing devices such as switches. Figure 2.2 also illustrates the switching capability of such structures. The frequency component at ω_1 is transmitted at low intensities, but is reflected strongly at higher intensities; while the frequency component at ω_2 is strongly reflected at low intensities, but is scarcely reflected at high intensities. Because of the combined effect from nonlinearity and periodicity, light waves at frequencies ω_1 and ω_2 become detuned from the Bragg condition at high intensities, changing their transmission characteristics. This property can be used to realize an optical switch.

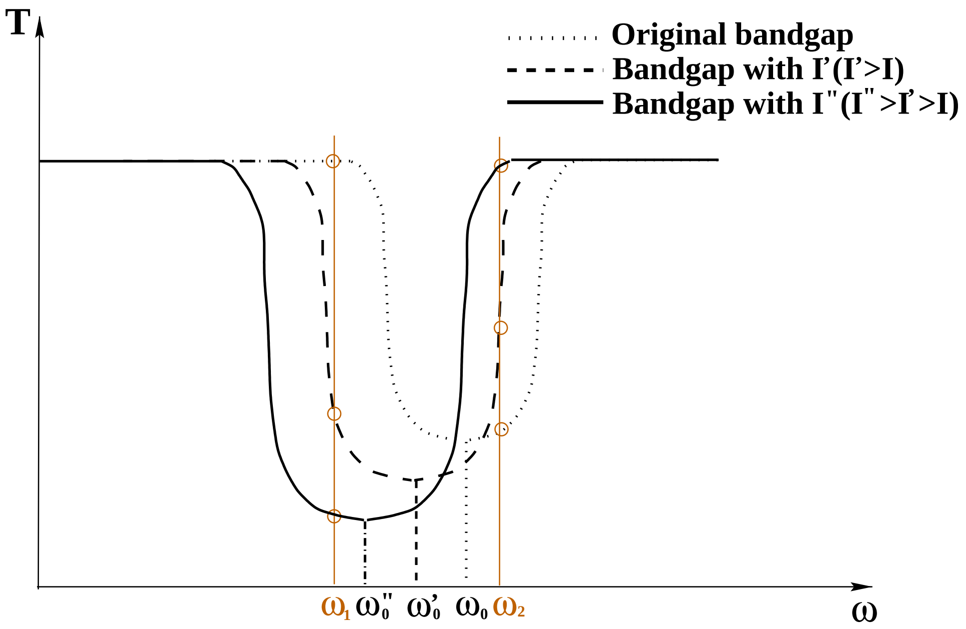

Figure 2.2: Intensity-dependent response of a nonlinear Bragg structure. It shows that the Bragg frequency ω_0 shifts to lower frequencies ω_0' and ω_0'' with increasing intensity. In addition, the size of the bandgap $\Delta\omega_{gap}$ increases with increasing intensity.

In addition to switching, nonlinear Bragg structures have been either theoretically predicted or experimentally demonstrated to provide limiting, pulse compression, and logic operations. In the next section, a review of the research work investigating the behavior of Bragg structures with a 3^{rd}-order nonlinearity is presented.

2.3 Previous Research on Nonlinear Periodic Signal Processing Devices

As explained in the preceding section, nonlinear periodic structures can potentially achieve multiple optical signal processing functions. Considerable past research effort has investigated various nonlinear periodic signal processing devices. The theoretical and experimental work is grouped under two categories: solitonic and non-solitonic propagation.

2.3.1 Solitonic Propagation

Studies of pulse propagation in nonlinear Bragg gratings have concentrated on *Bragg solitons*. Bragg solitons are solitary waves that propagate through a grating without changing their shapes. They arise from the balancing of the dispersion of the grating and the self-phase modulation due to the Kerr nonlinearity, and are predicted theoretically using nonlinear coupled-mode equations. *Gap solitons* represent the most studied class of Bragg solitons. These are Bragg solitons which have pulse spectra lying entirely within a photonic band gap [17, 18]. The term 'gap soliton' was first introduced in 1987 by Chen and Mills [19]; then Mills and Trullinger [20] proved the existence of gap solitons by analytic methods. Later, Sipe and Winful [21] and de Sterke and Sipe [22] showed that the electric field satisfies a nonlinear Schrödinger equation, which allows soliton solutions with carrier frequencies close to the edge of the stopband. Christodoulides and Joseph [23], and Aceves and Wabnitz [24] obtained soliton solutions with carrier frequencies close to the Bragg resonance.

Experiments with Bragg gratings have demonstrated soliton propagation, and more importantly, optical switching, and pulse compression. Sankey *et al.* [25] reported the first observation of all-optical switching in a nonlinear periodic structure using a corrugated silicon-on-insulator waveguide. They showed optical switching of a 5.5 μJ pulse with 50 ns duration at a wavelength $\lambda = 1.064$ μm. They demonstrated the concept described in Section 2.2.3 that pulses with frequencies in the stopband are detuned out of the gap because of the nonlinear effects, switching from a highly reflective state to a highly transmissive one. Switching between high- and low-reflectivity states implies these structures can serve as optical switching devices. Soon after Sankey *et al.*, Herbert *et al.* [8] observed optical power limiting in a three-dimensional colloidal array of microspheres immersed in a Kerr medium. These optical limiters transmit only low-intensity light but block high intensity radiation, and are useful in signal processing functions such as filtering, reshaping, and switching. In 1996, Eggleton *et al.* [18] reported a direct observation of soliton propagation and pulse compression in uniform fiber gratings, verifying experimentally for the first time the theories developed by Christodoulides and Aceves. This was followed by a further report [26], which both refined the experimental technique and broadened the experimental understanding of the dynamics of pulse propagation in these structures. Pulse compression was also later observed in nonuniform Bragg gratings by Broderick *et al.* [7]. Optical pulse compression in nonuniform gratings is attributed to two mechanisms: the optical pushbroom effect and cross phase modulation. The optical pushbroom effect requires a strong optical pump to alter the local refractive index. The pump-induced nonlinear index change creates a frequency shift at the trailing edge of the probe pulse. The consequent velocity increase of the trailing edge sweeps the probe energy to the front of the pulse, resulting in pulse compression. The change in index due to the pump also acts to detune the weak probe pulse from the center of the band gap, modifying the transmission of the probe [6]. The cross-phase modulation effect works in a similar fashion, except the probe pulse counter-propagates with the signal pulse [7].

2.3.2 Non-solitonic Propagation

Gap solitons are certainly of great interest for applications in telecommunications. However the strict requirements on peak power, pulse shape, and pulse duration needed to balance precisely the effects of dispersion and nonlinearity for producing a soliton may be difficult to satisfy.

Over the past years, studies of non-solitonic pulse propagation through multilayered structures with Kerr-type nonlinearities have attracted considerable attention. Scalora et al. [27] examined the nonlinear propagation of ultrashort pulses through a Kerr nonlinear quarter-wave Bragg reflector. They predicted numerically the possibility of ultrafast optical limiting and switching operations in such a structure. In these operations an increase in the optical field intensity changes the local refractive index due to the material nonlinearity (Eq. 1.1), shifting the entire stopband and making the system transparent at the initial Bragg stopband wavelengths. In order to achieve a higher switching contrast, a nonlinear coupled-cavity-type multilayered structure (NLCC) is proposed by Lee [28]. This new device consists of stacks of two half-wavelength cavity regions sandwiched by standard quarter-wavelength dielectric mirrors.

In 2000, Brzozowski *et al.* [9, 14] proposed a novel design of a nonlinear Bragg structure, one that consists of alternating layers of oppositely-signed Kerr materials. Figure 2.3 illustrates the proposed Bragg structure. This device is significantly different from periodic structures studied previously. The key to the novelty is the stability of the device due to the fact the nonlinearity of the structure is balanced precisely. None of the previous periodic structures have such configuration, therefore, they are not inherently stable. Here 'stable operation' means a single output depends solely on a single input (not the case in a bistable device). As a result of the balanced-nonlinearity, the average refractive

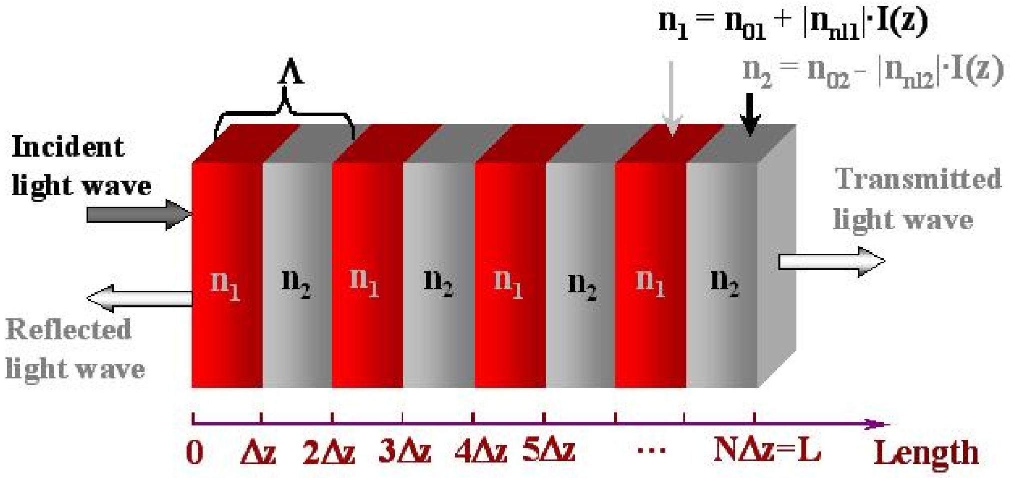

Figure 2.3: A schematic of a nonlinear Bragg grating with alternating oppositely-signed Kerr coefficients. Λ is the periodicity of the grating; $n_{01,02}$ are the linear refractive indices; $n_{nl1,nl2}$ are the Kerr coefficients of the two adjacent layers.

index $\bar{n}$, and thus the Bragg frequency (Eq. 2.3), remain fixed as intensity grows. The behavior of the device does not rely on the movement of stopband edges, but on the establishment of a stopband with intensity-invariant center frequency. Later, Pelinovsky *et al.* published two thorough theoretical steady-state analyses of this structure [10, 11]. The numerical analyses concluded that the device can perform stable all-optical limiting, even with small time-dependent perturbations [10]. Such optical limiters can be used to filter, shape, and multiplex optical pulses and to limit the optical power [29]. Additionally, optical limiters based on structural resonances – periodic alternations in the Kerr-coefficient – are distinct from other commonly used passive optical limiters exploiting self-focusing, two-photon absorption, and total internal reflection [30]. These limiters provide a usable reflected signal in addition to the transmitted signal. A complete set of logic functions using the transfer functions of the transmittance and reflectance was proven by Johnson *et al.* [31].

2.4 Thesis Objective

It is clear from the literature that nonlinear periodic structures represent a promising class of devices to enable a wide range of signal processing operations. Past research has concentrated on either soliton propagation or the steady-state analysis of nonlinear Bragg structures. The switching capabilities of Bragg solitons and the intensity limiting abilities for continuous waves have been studied in detail. However, the temporal behavior of one important class of nonlinear periodic structures – the stable nonlinear periodic devices with constant average refractive index – has been neglected. Furthermore, there has never been a complete investigation contrasting solitonic and non-solitonic propagation behavior in the same device. A systematic study identifying how ultrashort solitonic and non-solitonic pulses are processed in such stable devices remains to be carried out.

Present work considers the temporal behavior of the nonlinear Bragg grating device of Figure 2.3 with a focus on its applications in optical signal processing. The thesis seeks to address the following hitherto unanswered questions:

- in what ways do the proposed nonlinear Bragg structure provide an improvement to optical signal processing over previously considered devices?
- what are the important design issues in using nonlinear Bragg structures for practical optical signal processing?
- how does the time-dependent (pulse-processing) behavior relate to the known steady-state responses?
- what differentiates solitonic from non-solitonic propagation?

This is the first time-domain analysis of pulse propagation through a stable periodic structure with alternating oppositely-signed Kerr coefficients.

The subsequent chapters will thus characterize both qualitatively and quantitatively the non-solitonic propagation through a nonlinear Bragg structure, and then explore the response of the nonlinear periodic structure model proposed by Brzozowski *et al.* in the presence of a time-varying incident pulse. The transfer characteristic behavior is expected to be significantly different than that previously revealed through stationary analyses. Furthermore, the large spectral bandwidth of the ultrashort pulses in a time-domain analysis is expected to have further implications on both limiting behavior and pulse distortion.

2.5 Thesis Organization

The organization of the thesis is as follows:

In Chapter 3, the quantitative analytic framework is derived for subsequent deployment throughout the remainder of this thesis. The coupled-mode equations that describe the evolution of pulse envelopes in a nonlinear Bragg grating are derived. The Bragg soliton solutions of these coupled-mode equations are also obtained mathematically in this chapter. Chapter 4 describes the procedure for a convergent numerical solution of the equations derived. The numerical method for solving the coupled-mode system is explained. The boundary conditions and the balance equations for the system to be satisfied are identified. Also in this chapter, the Bragg structure studied in this thesis is defined and the material parameters chosen for the numerical simulations are stated and justified. Both solitonic (expressions defined in Chapter 3) and non-solitonic pulses are explained. Chapter 5 reports on three sets of time-domain analyses of ultrashort pulse propagation through different Bragg gratings with alternating oppositely-signed Kerr coefficients: (i) 0 linear grating; (ii) in-phase linear grating; (iii) out-of-phase linear grating. The term *in-phase linear grating* refers to as the case when the material with the higher linear index has a positive Kerr coefficient, and the material with the lower linear index has a negative Kerr coefficient. Similarly, the term *out-of-phase linear grating* means that the material with lower linear index has a positive Kerr coefficient, and the material with higher linear index has a negative Kerr coefficient. The numerical simulation results and the mechanisms behind the observations are discussed. The thesis concludes in Chapter 6 with an overview of the significant contributions made to optical signal processing and suggests future research directions.

Chapter 3

Analytical Model: Coupled-mode System

3.1 Introduction

Before exploring the time-domain signal processing capabilities of the device, it is necessary to return to the fundamentals to distill the essential elements of Maxwell's equations which require attention for understanding the evolution of pulses across a nonlinear periodic structure. Different sets of coupled-mode equations which describe the pulse propagation in nonlinear periodic structures have been derived previously for the study of gap solitons. The present chapter derives a set of coupled-mode equations which capture the physical mechanisms of one class of stable nonlinear periodic structures.

3.2 Approximation of the Refractive Index Function

The device under consideration consists of materials of alternating, oppositely-signed Kerr coefficients, as illustrated earlier in Figure 2.3. If the variations of the refractive index due to the combined effect of linear and nonlinear index differences in the constituent repeated subunits are much smaller than the average index, the index of refraction profile

$\mathbf{n_\Lambda(z, |E|^2)}$ can be approximately viewed as a periodic function along the spatial propagation direction of the structure, as illustrated in Figure 3.1. The function $\mathbf{n_\Lambda(z, |E|^2)}$ may be described analytically over one period, as follows:

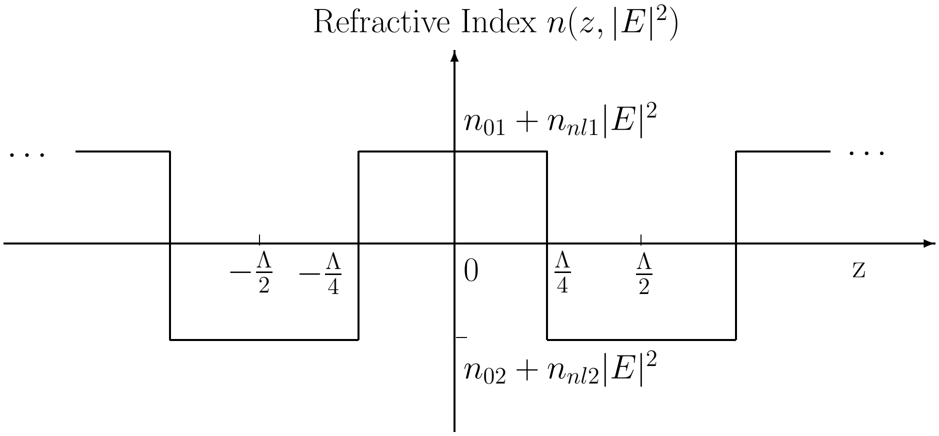

Figure 3.1: Refractive index profile of the Bragg grating device along the spatial propagation direction.

$$\mathbf{n_\Lambda(z, |E|^2)} = \begin{cases} n_{02} + n_{nl2}|E|^2, & \text{if } -\frac{n\Lambda}{2} < z < -\frac{n\Lambda}{4}; \\ n_{01} + n_{nl1}|E|^2, & \text{if } -\frac{n\Lambda}{4} < z < \frac{n\Lambda}{4}; \\ n_{02} + n_{nl2}|E|^2, & \text{if } \frac{n\Lambda}{4} < z < \frac{n\Lambda}{2};\ n = 1, 2, \ldots \end{cases} \tag{3.1}$$

with the periodic medium being a N-layered quarter-wave stack. By using a Fourier series expansion of this function, $\mathbf{n_\Lambda(z, |E|^2)}$ in Eq. (3.1) can be resolved into a infinite sum of sine and cosine terms:

$$\mathbf{n_\Lambda(z, |E|^2)} = a_0 + 2\sum_{n=1}^{\infty}[a_n \cos(2\pi n f_0 z) + b_n \sin(2\pi n f_0 z)], \tag{3.2}$$

where f_0 is the fundamental frequency: $f_0 = 1/\Lambda$. The coefficients of a_n and b_n represent the amplitudes of the even and odd terms, respectively. The quantity nf_0 represents the nth harmonic of the fundamental frequency f_0. The coefficient a_0 is the mean value of the periodic signal $\mathbf{n_\Lambda(z, |E|^2)}$ over one period, as shown by the time average:

$$a_0 = \frac{1}{\Lambda}\int_{-\Lambda/2}^{\Lambda/2} \mathbf{n_\Lambda(z, |E|^2)}dz \tag{3.3}$$

Coefficients a_n and b_n are:

$$\begin{aligned} a_n &= \frac{1}{\Lambda}\int_{-\Lambda/2}^{\Lambda/2} \mathbf{n_\Lambda}(\mathbf{z}, |\mathbf{E}|^{\mathbf{2}}) \cos{(2\pi n f_0 z)} dz, \qquad n = 1, 2, 3, \ \ldots \\ b_n &= \frac{1}{\Lambda}\int_{-\Lambda/2}^{\Lambda/2} \mathbf{n_\Lambda}(\mathbf{z}, |\mathbf{E}|^{\mathbf{2}}) \sin{(2\pi n f_0 z)} dz, \qquad n = 1, 2, 3, \ \ldots \end{aligned} \tag{3.4}$$

For an even function such as the one shown in Figure 3.1, it can be proven that $b_n = 0$ and $a_n \neq 0$. By substituting Eq. (3.1) into Eq. (3.3), we obtain

$$\begin{aligned} a_0 &= \frac{1}{\Lambda}\int_{-\Lambda/2}^{\Lambda/2} \mathbf{n_\Lambda}(\mathbf{z}, |\mathbf{E}|^{\mathbf{2}}) dz \\ &= \frac{2}{\Lambda}\left(\int_0^{\Lambda/4} (n_{01} + n_{nl1}|E|^2) dz + \int_{\Lambda/4}^{\Lambda/2} (n_{02} + n_{nl2}|E|^2) dz\right) \\ &= \frac{2}{\Lambda}\frac{\Lambda}{4}(n_{01} + n_{nl1}|E|^2 + n_{02} + n_{nl2}|E|^2) \\ &= \frac{n_{01} + n_{02}}{2} + \frac{n_{nl1} + n_{nl2}}{2}|E|^2 \end{aligned} \tag{3.5}$$

Similarly, the Fourier coefficient a_n can be evaluated as:

$$\begin{aligned} a_n &= \frac{1}{\Lambda}\int_{-\Lambda/2}^{\Lambda/2} \mathbf{n_\Lambda}(\mathbf{z}, |\mathbf{E}|^{\mathbf{2}}) \cos{(2\pi n f_0 z)} dz \\ &= \frac{2}{\Lambda}\int_0^{\Lambda/4} (n_{01} + n_{nl1}|E|^2) \cos(2\pi n f_0 z) dz \\ &\quad + \frac{2}{\Lambda}\int_{\Lambda/4}^{\Lambda/2} (n_{02} + n_{nl2}|E|^2) \cos(2\pi n f_0 z) dz \\ &= \frac{2}{\Lambda}\frac{\Lambda}{2\pi n}\left((n_{01} + n_{nl1}|E|^2) \sin(\frac{\pi n}{2}) - (n_{02} + n_{nl2}|E|^2) \sin(\frac{\pi n}{2})\right) \\ &= \frac{1}{\pi n}(n_{01} - n_{02} + n_{nl1}|E|^2 - n_{nl2}|E|^2) \sin(\frac{\pi n}{2}) \\ &= \begin{cases} 0, & \text{if } n \text{ is even} \\ \frac{1}{\pi n}(n_{01} - n_{02} + n_{nl1}|E|^2 - n_{nl2}|E|^2) \sin(\frac{\pi n}{2}), & \text{if } n \text{ is odd} \end{cases} \end{aligned} \tag{3.6}$$

Therefore, the index-of-refraction in Eq. (3.2) can be rewritten as:

$$\begin{aligned}\mathbf{n_\Lambda(z,|E|^2)} &= \frac{n_{01}+n_{02}}{2} + \frac{n_{nl1}+n_{nl2}}{2}|E|^2 \\ &+ 2\sum_{n=1,\,n\text{ odd}}^{\infty} \frac{1}{\pi n}(n_{01}-n_{02}+n_{nl1}|E|^2-n_{nl2}|E|^2)\sin(\frac{\pi n}{2})\cos(2\pi n f_0 z) \\ &\approx \frac{n_{01}+n_{02}}{2} + \frac{n_{nl1}+n_{nl2}}{2}|E|^2 + 2\left(\frac{n_{01}-n_{02}}{\pi} + \frac{n_{nl1}-n_{nl2}}{\pi}|E|^2\right)\cos\frac{2\pi z}{\Lambda}\end{aligned} \tag{3.7}$$

To simplify the above equation, four new parameters are introduced: linear index difference (n_{0k}), average Kerr coefficient (n_{nl}), average linear index (n_{ln}), and Kerr coefficient difference (n_{2k}):

$$\begin{aligned} n_{ln} &= \frac{n_{01}+n_{02}}{2}, \qquad & n_{nl} &= \frac{n_{nl1}+n_{nl2}}{2}, \\ n_{0k} &= \frac{n_{01}-n_{02}}{\pi}, \qquad & n_{2k} &= \frac{n_{nl1}-n_{nl2}}{\pi}. \end{aligned} \tag{3.8}$$

Defining the wave number k as $k = \frac{2\pi}{\Lambda}$, Eq. (3.7) can be rewritten as:

$$\mathbf{n_\Lambda(z,|E|^2)} = n_{ln} + n_{nl}|E|^2 + 2n_{0k}\cos kz + 2n_{2k}|E|^2\cos kz \tag{3.9}$$

3.3 Derivation of the Coupled-Mode Equations

The electromagnetic wave equation states:

$$\frac{\partial^2 E}{\partial z^2} - \frac{\mathbf{n^2(z,|E|^2)}}{c^2}\frac{\partial^2 E}{\partial t^2} = 0, \tag{3.10}$$

where $c = 1/\sqrt{\epsilon_0\mu_0}$ is the speed of light and $E(z,t)$ is the electric field.

$$E(z,t) = A_+(z,t)e^{i(k_0 z - \omega_0 t)} + A_-(z,t)e^{-i(k_0 z + \omega_0 t)} + \text{higher-order terms.} \tag{3.11}$$

$\omega_0 = ck_0/|n_{ln}|$ is the center frequency of a pulse, c is speed of light, and $k_0 = 2\pi|n_{ln}|/\lambda_0$ is the wave number of the light. A_+ and A_- are the slowly-varying envelope amplitudes of the incident and reflected waves. Peak reflectance occurs at the center of a forbidden band (λ_0) which can be written as $\lambda_0 = 2n_{ln}\Lambda$ from Eq. (2.1). In other words, resonance in the first bandgap occurs when $k = 2k_0$. Substituting Eq. (3.11) into Eq. (3.10), we obtain the first term as:

$$\begin{aligned}\frac{\partial^2 E}{\partial z^2} &= -k_0^2 A_+ e^{i(k_0 z - \omega_0 t)} + 2ik_0 \frac{\partial A_+}{\partial z} e^{i(k_0 z - \omega_0 t)} - k_0^2 A_- e^{-i(k_0 z + \omega_0 t)} \\ &+ 2ik_0 \frac{\partial A_-}{\partial z} e^{-i(k_0 z + \omega_0 t)} + \frac{\partial^2 E}{\partial z^2} e^{i(k_0 z - \omega_0 t)} + \frac{\partial^2 E}{\partial z^2} e^{-i(k_0 z + \omega_0 t)} \\ &\approx (-k_0^2 A_+ + 2ik_0 \frac{\partial A_+}{\partial z}) e^{i(k_0 z - \omega_0 t)} + (-k_0^2 A_- + 2ik_0 \frac{\partial A_-}{\partial z}) e^{-i(k_0 z + \omega_0 t)}, \\ &\text{(assuming the slowing varying envelope approximation)}\end{aligned} \tag{3.12}$$

and the second term in Eq. (3.10) becomes

$$\begin{aligned}\frac{\mathbf{n^2(z, |E|^2)}}{c^2} \frac{\partial^2 E}{\partial t^2} &\approx \frac{k_0}{\omega_0 n_{ln} c} [n_{ln}^2 + 2n_{ln} n_{nl} |E|^2 + (2n_{ln} n_{0k} + 2n_{ln} n_{2k} |E|^2)(e^{ikz} + e^{-ikz})] \frac{\partial^2 E}{\partial t^2} \\ &\text{(neglected all higher terms in } n_{2k}) \\ &= \frac{k_0}{\omega_0 c} [n_{ln} + 2n_{nl} |E|^2 + (2n_{ln} n_{0k} + 2n_{ln} n_{2k} |E|^2)(e^{i2k_0 z} + e^{-i2k_0 z})] \\ &\cdot [-\omega_0 (\omega_0 A_+ + 2i \frac{\partial A_+}{\partial t}) e^{i(k_0 z - \omega_0 t)} - \omega_0 (\omega_0 A_- + 2i \frac{\partial A_-}{\partial t}) e^{-i(k_0 z + \omega_0 t)}].\end{aligned} \tag{3.13}$$

The intensity term $|E|^2$ in the above equation can be expressed in terms of A_+ and A_- as:

$$|E|^2 = E \cdot E^* = |A_+|^2 + |A_-|^2 + A_+ A_-^* e^{i2k_0 z} + A_+^* A_- e^{-i2k_0 z}. \tag{3.14}$$

Then Eq. (3.13) can be simplified to:

$$\begin{aligned}\frac{\mathbf{n^2(z, |E|^2)}}{c^2} \frac{\partial^2 E}{\partial t^2} \approx & -\frac{k_0}{c} [n_{ln} \omega_0 A_+ + 2in_{ln} \frac{\partial A_+}{\partial t} + 2n_{0k} \omega_0 A_- + 2n_{nl} (|A_+|^2 + |A_-|^2) \omega_0 A_+ \\ & + 2n_{nl} A_+ A_-^* \omega_0 A_- + 2n_{2k} (|A_+|^2 + |A_-|^2) \omega_0 A_- + 2n_{2k} A_+^* A_- \omega_0 A_+ \\ & + 2n_{2k} A_+ A_-^* \omega_0 A_+] \cdot e^{i(k_0 z - \omega_0 t)} - \frac{k_0}{c} [n_{ln} \omega_0 A_- + 2in_{ln} \frac{\partial A_-}{\partial t} \\ & + 2n_{0k} \omega_0 A_+ + 2n_{nl} (|A_+|^2 + |A_-|^2) \omega_0 A_- + 2n_{nl} A_+^* A_- \omega_0 A_+ \\ & + 2n_{2k} (|A_+|^2 + |A_-|^2) \omega_0 A_+ + 2n_{2k} A_+ A_-^* \omega_0 A_- + 2n_{2k} A_+^* A_- \omega_0 A_-] \\ & \cdot e^{-i(k_0 z + \omega_0 t)}.\end{aligned} \tag{3.15}$$

Thus, Eq. (3.10) can be represented in terms of A_+ and A_- by combining Eq. (3.12) and (3.15). If we group all the $e^{i(k_0z-\omega_0t)}$ terms, we obtain

$$-k_0^2A_+ + 2ik_0\frac{\partial A_+}{\partial z} + \frac{k_0}{c}[n_{ln}\omega_0A_+ + 2in_{ln}\frac{\partial A_+}{\partial t} + 2n_{0k}\omega_0A_- + 2n_{nl}(|A_+|^2+|A_-|^2)\omega_0A_+$$
$$+2n_{nl}A_+A_-^*\omega_0A_- + 2n_{2k}(|A_+|^2+|A_-|^2)\omega_0A_- + 2n_{2k}A_+^*A_-\omega_0A_+ + 2n_{2k}A_+A_-^*\omega_0A_+] = 0. \tag{3.16}$$

Using product expansions and simplification, the above equation becomes

$$\begin{aligned} &i\frac{c}{\omega_0}\frac{\partial A_+}{\partial z} + i\frac{n_{ln}}{\omega_0}\frac{\partial A_+}{\partial t} + n_{0k}A_- + n_{nl}(|A_+|^2+|A_-|^2)A_+ + n_{nl}|A_-|^2A_+ \\ &+ n_{2k}(|A_+|^2+|A_-|^2)A_- + n_{2k}|A_+|^2A_- + n_{2k}A_+^2A_-^* = 0. \end{aligned} \tag{3.17}$$

Similarly, by grouping all the $e^{-i(k_0z+\omega_0t)}$ terms, we obtain the second coupled-mode equation:

$$\begin{aligned} &-i\frac{c}{\omega_0}\frac{\partial A_-}{\partial z} + i\frac{n_{ln}}{\omega_0}\frac{\partial A_-}{\partial t} + n_{0k}A_+ + n_{nl}(|A_+|^2+|A_-|^2)A_- + n_{nl}|A_+|^2A_- \\ &+ n_{2k}(|A_+|^2+|A_-|^2)A_+ + n_{2k}|A_-|^2A_+ + n_{2k}A_-^2A_+^* = 0. \end{aligned} \tag{3.18}$$

To simplify the two coupled-mode equations (Eq. 3.17 and 3.18) further, the spatial coordinate Z and time parameter T are introduced, where $Z = \omega_0z/c$ and $T = \omega_0t/n_{ln}$. This process of parameter normalization ensures the spatial and time parameters are of the same unit; hence making the numerical analysis easier. The resulting normalized coupled-mode equations are:

$$i\left(\frac{\partial A_+}{\partial Z} + \frac{\partial A_+}{\partial T}\right) + n_{0k}A_- + n_{nl}(|A_+|^2+2|A_-|^2)A_+ + n_{2k}[(2|A_+|^2+|A_-|^2)A_- + A_+^2A_-^*] = 0, \tag{3.19}$$

$$-i\left(\frac{\partial A_-}{\partial Z} - \frac{\partial A_-}{\partial T}\right) + n_{0k}A_+ + n_{nl}(2|A_+|^2+|A_-|^2)A_- + n_{2k}[(|A_+|^2+2|A_-|^2)A_+ + A_-^2A_+^*] = 0. \tag{3.20}$$

These two coupled-mode equations describe the evolution of the electric field envelope (forward wave A_+ and backward wave A_-).

3.4 Exact Soliton Solutions

Since the propagation behavior of solitonic and non-solitonic pulses will be compared in the next chapter, it is important to derive the exact solutions of the coupled-mode system (3.19)–(3.20) for gap solitons. We collaborated with with Professor D. Pelinovsky from McMaster University to obtain the soliton solutions.

The gap solitons exist in the system when $n_{nl} = 0$, $n_{0k} < 0$, $n_{2k} > 0$, or alternatively when $n_{nl} = 0$, $n_{0k} > 0$, $n_{2k} < 0$. The parameter n_{2k} can be normalized to be positive without loss of generality. In order to find exact solutions for gap solitons when $n_{nl} = 0$, we adopt relativistic Lorentz transformations of the coordinates, giving:

$$\zeta = \frac{Z - VT}{\sqrt{1 - V^2}}, \qquad \tau = \frac{T - VZ}{\sqrt{1 - V^2}}, \qquad A_\pm(Z, T) = \sqrt{1 \pm V} a_\pm(\zeta, \tau). \tag{3.21}$$

The coupled-mode system (3.19) – (3.20) in these new coordinates then takes the form:

$$i\left(\frac{\partial a_+}{\partial \zeta} + \frac{\partial a_+}{\partial \tau}\right) + n_{0k} a_- + n_{2k}\left[\left(2(1+V)|a_+|^2 + (1-V)|a_-|^2\right) a_- + (1+V) a_+^2 \bar{a}_-\right] = 0, \tag{3.22}$$

$$-i\left(\frac{\partial a_-}{\partial \zeta} - \frac{\partial a_-}{\partial \tau}\right) + n_{0k} a_+ + n_{2k}\left[\left((1+V)|a_+|^2 + 2(1-V)|a_-|^2\right) a_+ + (1-V) a_-^2 \bar{a}_+\right] = 0. \tag{3.23}$$

Gap solitons are stationary solutions of the coupled-mode system (3.19)–(3.20) that move with a constant velocity V and have a constant detuning frequency Ω. Separating variables in the system (3.22)–(3.23), we write these stationary solutions in the form:

$$a_+ = \sqrt{Q(\zeta)} e^{i(\phi(\zeta) - \psi(\zeta)) + i\Omega\tau}, \qquad a_- = \sqrt{Q(\zeta)} e^{i\phi(\zeta) + i\Omega\tau}. \tag{3.24}$$

The function $Q(\zeta)$ in (3.24) is the intensity of the right-propagating and left-propagating waves, i.e. $Q(\zeta) = |a_+|^2(\zeta) = |a_-|^2(\zeta)$, where $a_\pm(\zeta, \tau)$ satisfies zero boundary conditions in ζ. The functions $(\phi(\zeta) - \psi(\zeta))$ and $\psi(\zeta)$ in (3.24) are the complex phases of the waves, given that $\psi(\zeta)$ represents the phase difference between the complex phases. It follows from Eqs. (3.22), (3.23), and (3.24) that the functions $Q(\zeta)$ and $\psi(\zeta)$ satisfy the planar

Hamiltonian system:

$$\frac{\partial Q}{\partial \zeta} = \frac{\partial H}{\partial \psi} = -2Q \sin\psi \left(n_{0k} + 2n_{2k}Q\right), \tag{3.25}$$

$$\frac{\partial \psi}{\partial \zeta} = -\frac{\partial H}{\partial Q} = 2\Omega - 2\cos\psi \left(n_{0k} + 4n_{2k}Q\right), \tag{3.26}$$

where the Hamiltonian $H = H(Q, \psi)$ is given by:

$$H = 2Q \left(n_{0k} + 2n_{2k}Q\right) \cos\psi - 2\Omega Q. \tag{3.27}$$

The gap soliton solution satisfies the zero boundary conditions at infinity: $Q(\zeta) \to 0$ as $|\zeta| \to \infty$. Such solutions occur for $H = 0$ in Eq. (3.27), requiring:

$$\cos\psi = \frac{\Omega}{n_{0k} + 2n_{2k}Q}. \tag{3.28}$$

The closed-form solution of the system (3.25)–(3.26) can be then written as:

$$\left(\frac{\partial Q}{\partial \zeta}\right)^2 + U(Q) = 0, \qquad \text{where } \mathrm{U(Q) = -4Q^2\left[(n_{0k} + 2n_{2k}Q)^2 - \Omega^2\right]}. \tag{3.29}$$

The system (3.29) describes the zero energy level of a particle moving in a potential field $U(Q)$. The critical point $Q = 0$ is a saddle point if $U''(0) < 0$, which necessitates $|\Omega| < |n_{0k}|$. Under this constraint, the trajectory of the solution $Q = Q(\zeta)$ starts from $Q = 0$ in the limit $\zeta = -\infty$, grows exponentially until the turning point $Q = Q_{sol}$, where $U(Q_{sol}) = 0$, and then decays exponentially to $Q = 0$ in the limit $\zeta \to +\infty$. If $n_{2k} > 0$ and $n_{0k} < 0$, the turning point exists at

$$Q_{sol} = \frac{|n_{0k}| - |\Omega|}{2n_{2k}}.$$

The analytical expression for the gap soliton can be derived from Eq. (3.29) and is found to take the form:

$$Q(\zeta) = \frac{n_{0k}^2 - \Omega^2}{2n_{2k}(|\Omega| \cosh\gamma\zeta + |n_{0k}|)}, \tag{3.30}$$

where $\gamma = 2(n_{0k}^2 - \Omega^2)^{1/2}$. The gap soliton is centered at $\zeta = 0$, where $Q(0) = Q_{sol}$, and it is exponentially localized, such that $Q(\zeta) \to Q_\infty e^{-\gamma|\zeta|}$ as $|\zeta| \to \infty$.

The gap soliton solution (Eq. 3.30) exists for $n_{2k} > 0$, $n_{0k} < 0$ and $0 \neq |\Omega| < |n_{0k}|$, i.e., when the nonlinear grating has an out-of-phase built-in modulation of the linear refractive index. The term *out-of-phase grating* is referred to as the case when the material with the lower linear index has a positive Kerr coefficient, and the material with the higher linear index has a negative Kerr coefficient.

3.5 Summary

In this chapter, a system of coupled-mode equations were developed for wave amplitudes in time and space based on a Fourier series expansion of linear and nonlinear refractive indices in a nonlinear periodic structure. The coupled-mode equations derived here are rearranged for the special stable class of nonlinear periodic structures consisting of alternating Kerr nonlinear materials. In the next chapter, a simulation model built based upon this system is described.

Chapter 4

Numerical Model: Derivation and Validation

4.1 Introduction

In the previous chapter, the system of coupled-mode equations for nonlinear periodic structures was developed analytically. This chapter presents the numerical techniques employed in solving the system and asserts the range of physically important material parameters.

4.2 Numerical Method for Solving the CME System

The complex envelope function of the forward and backward propagating waves can be decomposed into its real and imaginary parts:

$$A_+ = u + iw, \qquad A_- = v + iy. \tag{4.1}$$

The real functions u, v, w, and y satisfy the coupled system (3.19) – (3.20), and therefore are given by:

$$
\begin{aligned}
\frac{\partial u}{\partial T}+\frac{\partial u}{\partial Z}+n_{0k}y+f(u,w,v,y)&=0,\\
-\frac{\partial w}{\partial T}-\frac{\partial w}{\partial Z}+n_{0k}v+f(w,u,y,v)&=0,\\
\frac{\partial v}{\partial T}-\frac{\partial v}{\partial Z}+n_{0k}w+f(v,y,u,w)&=0,\\
-\frac{\partial y}{\partial T}+\frac{\partial y}{\partial Z}+n_{0k}u+f(y,v,w,u)&=0, \qquad (4.2)
\end{aligned}
$$

where the nonlinear function $f(u,w,v,y)$ is defined by

$$f(u,w,v,y)=n_{nl}(u^2+w^2+2v^2+2y^2)w+n_{2k}[(u^2+3w^2+v^2+y^2)y+2uwv]. \qquad (4.3)$$

Assuming the nonlinear functions $f(u,w,v,y)$, $f(w,u,y,v)$, $f(v,y,u,w)$, and $f(y,v,w,u)$ are small, the partial differential equations system in Eq. (4.2) can be further reduced to:

$$
\begin{aligned}
\frac{\partial^2 u}{\partial T^2}-\frac{\partial^2 u}{\partial Z^2}+n_{0k}^2u&=0,\\
\frac{\partial^2 w}{\partial T^2}-\frac{\partial^2 w}{\partial Z^2}+n_{0k}^2w&=0,\\
\frac{\partial^2 v}{\partial T^2}-\frac{\partial^2 v}{\partial Z^2}+n_{0k}^2v&=0,\\
\frac{\partial^2 y}{\partial T^2}-\frac{\partial^2 y}{\partial Z^2}+n_{0k}^2y&=0. \qquad (4.4)
\end{aligned}
$$

To solve these numerically, a finite-difference method is used, where the functions u, v, w, and y are calculated based on the number of mesh points taken in both time and space:

$$
\begin{aligned}
Z &= \alpha\cdot\Delta z, &&\text{where } \alpha=0,1,\ldots,N,N+1, \text{ and the space step size } \Delta z=\frac{L}{N+1};\\
T &= \beta\cdot\Delta t, &&\text{where } \beta=0,1,\ldots,K, \text{ and } \Delta t \text{ is the time step size.}
\end{aligned}
$$

The functions $u(Z,T)$, $v(Z,T)$, $w(Z,T)$, and $y(Z,T)$ can be thought of as two-dimensional vectors, with time and space dimensions. For example,

$$u(Z,T) = \begin{bmatrix} u_0^0 & u_{1dt}^0 & u_{2\Delta t}^0 & \cdots & u_{K\Delta t}^0 \\ u_0^{1\Delta z} & u_{1\Delta t}^{1\Delta z} & u_{2\Delta t}^{1\Delta z} & \cdots & u_{K\Delta t}^{1\Delta z} \\ \vdots & \vdots & \vdots & \vdots & \vdots \\ u_0^{N\Delta z} & u_{1\Delta t}^{N\Delta z} & u_{2\Delta t}^{N\Delta z} & \cdots & u_{K\Delta t}^{N\Delta z} \\ u_0^{(N+1)\Delta z} & u_{1\Delta t}^{(N+1)\Delta z} & u_{2\Delta t}^{(N+1)\Delta z} & \cdots & u_{K\Delta t}^{(N+1)\Delta z} \end{bmatrix}$$

with each element $u_{\beta\Delta t}^{\alpha\Delta z}$ in the array represents the value of the function u at the grid point $(Z = \alpha\Delta z, T = \beta\Delta t)$. For simplicity, the term $u_{\beta\Delta t}^{\alpha\Delta z}$ is written as u_β^α from here on.

The Crank-Nicholson finite difference method is used to solve the partial differential equations defined in Eq. (4.2). The two-dimensional partial differential equations (i.e., $\frac{\partial u(Z,T)}{\partial T}$ and $\frac{\partial u(Z,T)}{\partial Z}$) evaluated at a grid point $(Z = \alpha\Delta z, T = \beta\Delta t)$ can be approximated as

$$\begin{aligned} \frac{\partial u}{\partial T} &= \frac{u_{\beta+1}^\alpha - u_{\beta-1}^\alpha}{2\Delta t}; && (4.5) \\ \frac{\partial u}{\partial Z} &= \frac{1}{2}\left[\frac{\partial u_{\beta+1}^\alpha}{\partial Z} + \frac{\partial u_{\beta-1}^\alpha}{\partial Z}\right] = \frac{u_{\beta+1}^{\alpha+1} - u_{\beta+1}^{\alpha-1}}{4\Delta z} + \frac{u_{\beta-1}^{\alpha+1} - u_{\beta-1}^{\alpha-1}}{4\Delta z}. && (4.6) \end{aligned}$$

The partial derivatives of the functions $w(Z,T)$, $v(Z,T)$, and $y(Z,T)$ are approximated in a similar manner. This numerical method is known to be unconditionally stable [11] for any values of Δt, Δz, and n_{0k}. Thus, a linear system is obtained for solving the functions at a specific time instance:

$$\left\{ \begin{aligned} &\begin{bmatrix} A(\frac{\Delta t}{2\Delta z}) & C \\ -D & B(\frac{\Delta t}{2\Delta z}) \end{bmatrix} \begin{bmatrix} u_\beta^{\alpha+1} \\ y_\beta^{\alpha+1} \end{bmatrix} = \begin{bmatrix} A(-\frac{\Delta t}{2\Delta z}) & -C \\ D & B(-\frac{\Delta t}{2\Delta z}) \end{bmatrix} \begin{bmatrix} u_\beta^{\alpha-1} \\ y_\beta^{\alpha-1} \end{bmatrix} + \begin{bmatrix} H_\beta^\alpha(u,w,v,y) \\ H_\beta^\alpha(w,u,y,v) \end{bmatrix} \\ &\begin{bmatrix} A(\frac{\Delta t}{2\Delta z}) & -C \\ D & B(\frac{\Delta t}{2\Delta z}) \end{bmatrix} \begin{bmatrix} w_\beta^{\alpha+1} \\ v_\beta^{\alpha+1} \end{bmatrix} = \begin{bmatrix} A(-\frac{\Delta t}{2\Delta z}) & C \\ -D & B(-\frac{\Delta t}{2\Delta z}) \end{bmatrix} \begin{bmatrix} w_\beta^{\alpha-1} \\ v_\beta^{\alpha-1} \end{bmatrix} + \begin{bmatrix} H_\beta^\alpha(v,y,u,w) \\ H_\beta^\alpha(y,v,w,u) \end{bmatrix} \end{aligned} \right. \qquad (4.7)$$

The full derivation of the above linear system is included in Appendix A. The expressions of the matrices A, B, C, D, and H are also stated there.

The complicated coupled-mode system described in Chapter 3 can be now estimated by using the non-iterative algorithm expressed in Eq. (4.7). This makes the numerical computations of the envelope functions u, v, w, and y much simpler.

4.3 Boundary Conditions and Balance Equations

By assumption, the input pulse $I_{in}(T)$ is incident from the left end. The boundary conditions therefore are defined as:

$$\begin{aligned} u_\beta^0 = \sqrt{I_{in}(T)}\cos\theta_{in}(T), \qquad & w_\beta^0 = \sqrt{I_{in}(T)}\sin\theta_{in}(T), \\ v_\beta^{N+1} = 0, \qquad & y_\beta^{N+1} = 0, \end{aligned} \tag{4.8}$$

where $I_{in}(T)$ and $\theta_{in}(T)$ represent the amplitude and phase modulation of the incident pulse launched at the grating, respectively, at a specific time instance T. Eq. (4.8) can be rearranged by using the relationship in Eq. (4.1) as follows:

$$\begin{aligned} I_{in}(T) &= |A_+(Z=0,T)|^2, \qquad I_{ref}(T) = |A_-(Z=0,T)|^2, \\ I_{tran}(T) &= |A_+(Z=L,T)|^2, \qquad |A_-(Z=L,T)|^2 = 0, \end{aligned} \tag{4.9}$$

where $I_{ref}(T)$ is the intensity of the input light wave at the input end of the grating (left end), and $I_{tran}(T)$ is the intensity at the output (right end). The reflected and transmitted intensities $I_{ref}(T)$ and $I_{tran}(T)$ are generated dynamically through the time-dependent solutions of the coupled-mode system (3.19)–(3.20).

The boundary conditions defined in Eq. (4.9) are satisfied at all times. In addition to this restriction, the coupled-mode system (3.19)–(3.20) obeys the balance equations:

$$\frac{\partial}{\partial T}\left(|A_+|^2 + |A_-|^2\right) + \frac{\partial}{\partial Z}\left(|A_+|^2 - |A_-|^2\right) = 0. \tag{4.10}$$

Integrating over the nonlinear structure, a balance between the incident, reflected, and transmitted intensities can be obtained:

$$\frac{d}{dT}\int_0^L \left(|A_+|^2 + |A_-|^2\right) dZ = I_{in}(T) - I_{ref}(T) - I_{tran}(T).$$

If the incident pulse is fully transmitted and no light becomes trapped within the grating, the conservation of total energy density ($\mathcal{W}$), in the limit $T \to \infty$, takes the form:

$$\mathcal{W}_{in} = \mathcal{W}_{ref} + \mathcal{W}_{tran}, \qquad \text{where } \mathcal{W}_{in} = \int_{-\infty}^{\infty} I_{in}(T) dT. \tag{4.11}$$

where $\mathcal{W}$ denotes the total incident, reflected, or transmitted energy density. This balance between total intensities enables the computation of the input-output transmission characteristic for a pulse, $\mathcal{W}_{tran} = \mathcal{W}_{tran}(\mathcal{W}_{in})$.

4.4 The Nonlinear Bragg Structure Model

The device under consideration in this work is a nonlinear Bragg structure which consists of alternating layers of oppositely-signed Kerr materials [9]. This structure was briefly introduced earlier in Chapter 2 (Figure 2.3).

An incident pulse is assumed to be launched at the left end of the structure. The boundary conditions defined in Eq. 4.9 are satisfied at all times. In addition, zero initial conditions are assumed: $A_{\pm}(Z, T = 0) = 0$. For most of the simulations, a Gaussian pulse is considered as the input to the system:

$$I_{in}(T) = I_{peak}\, e^{-\frac{(T-\mu)^2}{2\sigma^2}}, \tag{4.12}$$

where I_{peak} is the maximum intensity of the pulse, μ is the time-delay of the pulse, and σ defines the pulse duration as the full width at half maximum, or $FWHM$:

$$FWHM = 2\sigma\sqrt{2\ln 2}. \tag{4.13}$$

If $\mu \gg FWHM$, the pulse intensities approach zero at $T = 0$ and the small mismatch between the pulse intensity $I_{in}(0)$ and the zero initial condition at $T = 0$ is neglected.

4.4.1 Material Parameters Justification

This section discusses the physical approximations behind the derivation of the coupled-mode system (3.19)–(3.20), and justifies the choice of material parameters n_{0k} and n_{2k}

in the numerical modeling of the system.

In deriving the coupled-mode system (3.19)–(3.20), it is assumed that the response time of the optical material is much smaller than the duration of the pulse envelope. Also, in the present work, a maximum index change of 0.01 is assumed. Experimentally, refractive index changes as large as 0.1 have been obtained. Ultrafast index changes have been reported in systems such as polymers doped with azobenzenes, low temperature grown GaAs, or Helium-plasma-assisted molecular beam epitaxy InGaAsP [32, 33, 34, 35]. The response time of the materials was reported to be as fast as 2 ps [33, 34].

In deriving the coupled-mode equations (3.19)–(3.20), the effects of absorption are also neglected. In reality, materials which exhibit index changes as large as 0.1 have significant linear absorption. Devices made from such highly nonlinear materials would need to be at least two microns thick to give rise to the class of transfer functions considered herein. Over such length a device would lose up to 50% of the transmitted power as a result of absorption. This effect would limit the performance of the optical device. In simulations reported herein, the absorption effects are not included because they do not change the qualitative behavior. It is also noted that index changes of 0.01 can be obtained at spectral points at which the absorption is lowered by orders of magnitude [36].

The specific devices considered herein assume significant control over the values of both the Kerr coefficient (oppositely-signed) and linear indices of the materials. In a two-level system with a single absorption resonance, the sign of the Kerr coefficient is positive for wavelengths shorter than the wavelength of maximum absorption and for wavelengths longer than the wavelength of maximum two-photon absorption [16]. For wavelengths in between these two regions the sign of Kerr coefficient is negative [37]. Thus, for any two nonlinear materials with single absorption resonances at different spectral positions there exists a spectral range where the Kerr nonlinearities are of opposite sign. Also, index-matching techniques can be used to enable control over the value of the linear index. For example, a combination of polymers in correct proportions can be used in organic systems in order to obtain the desired bulk refractive index. In the case of compound semiconductors, a change in the composition tunes the linear refractive index.

Throughout the simulations reported herein, the Kerr coefficients $n_{nl1,2}$ of the two adjacent layers are assumed to be $n_{nl1,2} = \pm 2.5 \times 10^{-12}$ cm^2/W, and the average linear index $n_{ln} = (n_{01} + n_{02})/2$ is fixed at 1.50. The center frequency of the incident pulse is assumed fixed at $f_0 = 2 \times 10^{14}$ Hz (or at wavelength $\lambda_0 = 1.50$ μm). These choices give the values $n_{nl} = 0$ and $n_{2k} = \frac{1}{2\pi} \times 10^{-11}$ cm^2/W in the coupled-mode system (3.19)–(3.20).

4.5 Numerical Model Validation and First Exploration

This section describes the evolution of pulse shape and spectrum when short optical pulses propagate through the nonlinear Bragg structure. In general, Kerr nonlinearity-induced self-phase modulation and grating-generated dispersion occur simultaneously, and both tend to modify the shapes of the propagating optical pulses. However, under certain circumstances, an exact cancellation of these two effects can occur, allowing the Bragg soliton to propagate through large distances with no change in shape. Given the availability of the analytical solutions of the Bragg soliton, the simulations presented in this section serve to validate the numerical model.

In Section 3.3, the soliton solutions to the coupled-mode system were derived. The propagation of a Bragg soliton with its shape defined in Eq. (3.30) is simulated here to compare with its known properties to validate the numerical model. Device parameters of $n_{nl} = 0$, $n_{2k} = \frac{1}{2\pi} \times 10^{-11}$ cm^2/W, and $n_{0k} = -0.1$ are used in the coupled-mode system (3.19)–(3.20). The parameters of the Bragg solitons are chosen as: $I_{\text{peak}} = 55$ GW/cm^2, input soliton pulse $FWHM \approx 27$ fs, the constant velocity factor $V = 0.5$, and the detuning frequency $\Omega = 0.01$. The intensities of the forward and backward waves $|A_{\pm}|^2$ for a propagating Bragg soliton are simulated and shown in Figure 4.1(a) and 4.1(b) below. The Bragg soliton propagates with a constant speed V and a constant detuning

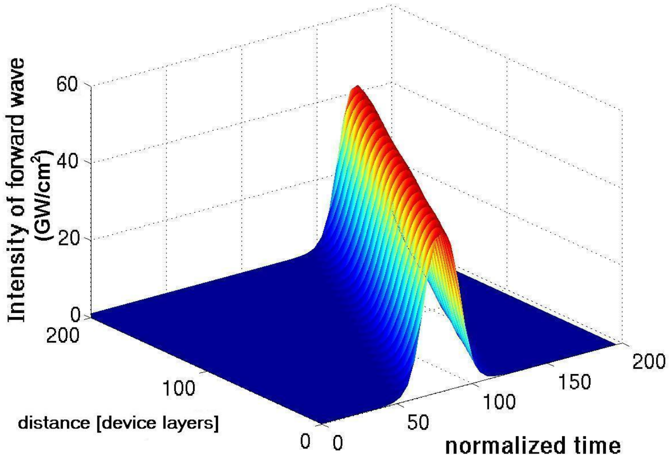

(a)

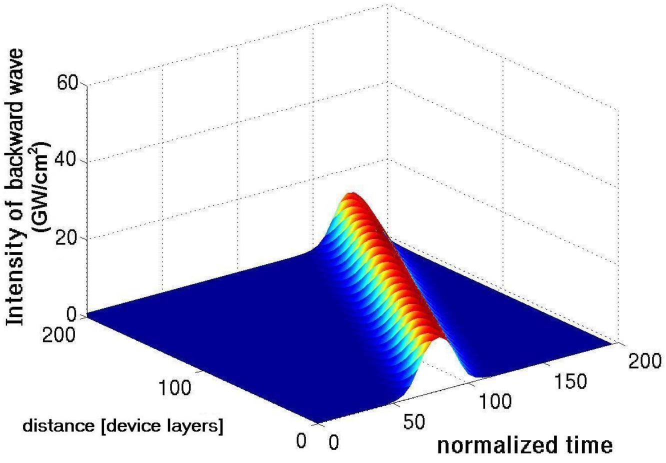

(b)

Figure 4.1: Bragg soliton propagation simulated using the system (3.19)–(3.20) with $n_{nl} = 0$, $n_{0k} = -0.1$, and $n_{2k} = \frac{1}{2\pi} \times 10^{-11}$ cm^2/W. Shown are (a) the intensity of the forward wave and (b) the intensity of the backward wave. The parameters of the Bragg soliton are: $I_{\text{peak}} = 55$ GW/cm^2 and $FWHM \approx 27$ fs.

frequency Ω from the center of the stopband frequency ω_0. The amplitude envelope of both forward and backward propagating waves remain constant spatially. Thus steady propagation of Bragg solitons is observed in devices with large L.

For comparison, the propagation of a non-solitonic pulse (a Gaussian pulse defined in Eq. 4.12) with $I_{\text{peak}} = 55$ GW/cm^2 and $FWHM = 27$ fs through the same device is simulated to illustrate the effect of imbalance between self-phase modulation and dispersion. Two scenarios of Gaussian pulse propagation are observed, depending on the parameter n_{0k} which represents the strength of the linear index grating along the structure. If $n_{0k} = 0$, the pulse amplitude decays and the pulse width grows over the propagation distance. This scenario is shown in Figure 4.2. If $n_{0k} = -0.1$ (the same device as in the soliton case in Figure 4.1), the pulse amplitude experiences strong compression, pulse reshaping and high-amplitude multiple-peak oscillations. This scenario is shown in Figure 4.3. Pulse compression–decompression cycling is observed in the system (3.19)–(3.20) in the case when $n_{0k} < 0$ (Bragg soliton propagation is possible); and pulse amplitude decay is observed when $n_{0k} \geq 0$ (Bragg soliton propagation is not allowed).

To summarize, a gap soliton (Eq. 3.24) propagates through the periodic structure as a uniformly shaped soliton pulse in both coupled counter-propagating waves. When a non-solitonic pulse (Eq. 4.12) is launched at the input of the optical device, it could also evolve into a gap soliton. In the case when the system does not support solitons, pulse propagates as a forward wave, generates a reflected backward wave, therefore exhibits non-solitonic behavior: the pulse amplitude decays, or the pulse compresses, gets reshaped and oscillates.

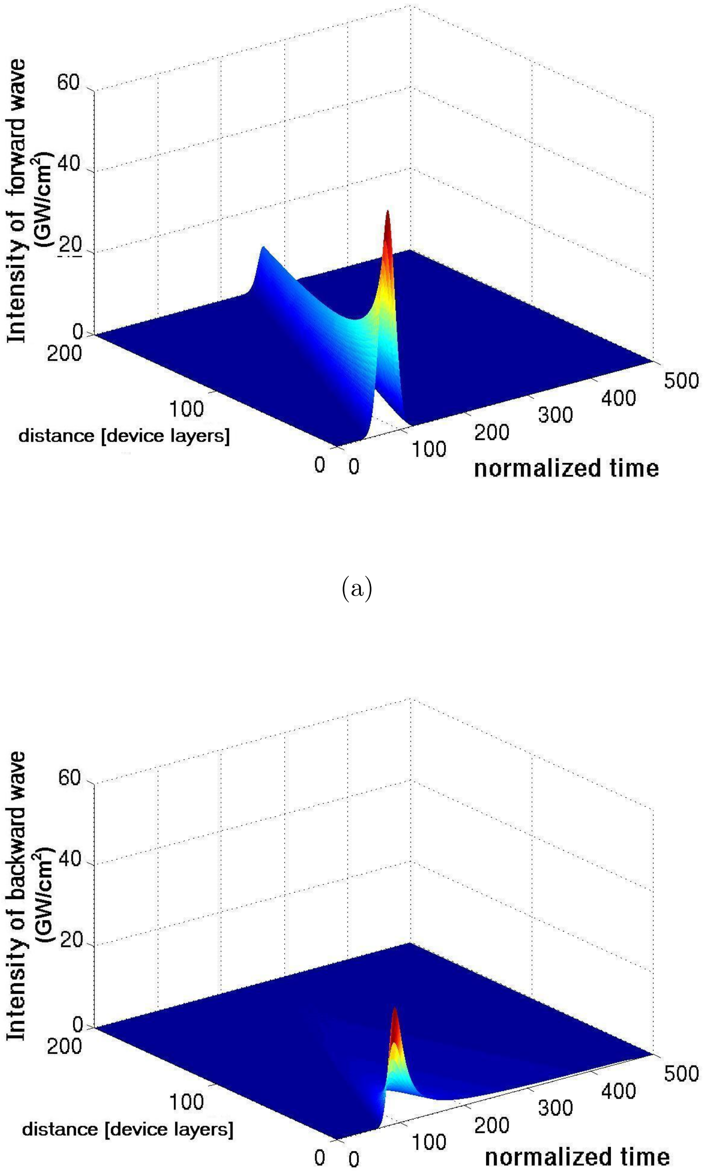

(a)

(b)

Figure 4.2: Decaying Gaussian pulse propagates in the same structure as in Figure 4.1, but without a built-in linear grating ($n_{0k} = 0$). Shown are (a) the intensity of the forward wave and (b) the intensity of the backward wave. The parameters of the Gaussian pulse are: $I_{\text{peak}} = 55$ GW/cm^2 and $FWHM = 27$ fs to match the Bragg soliton in Figure 4.1.

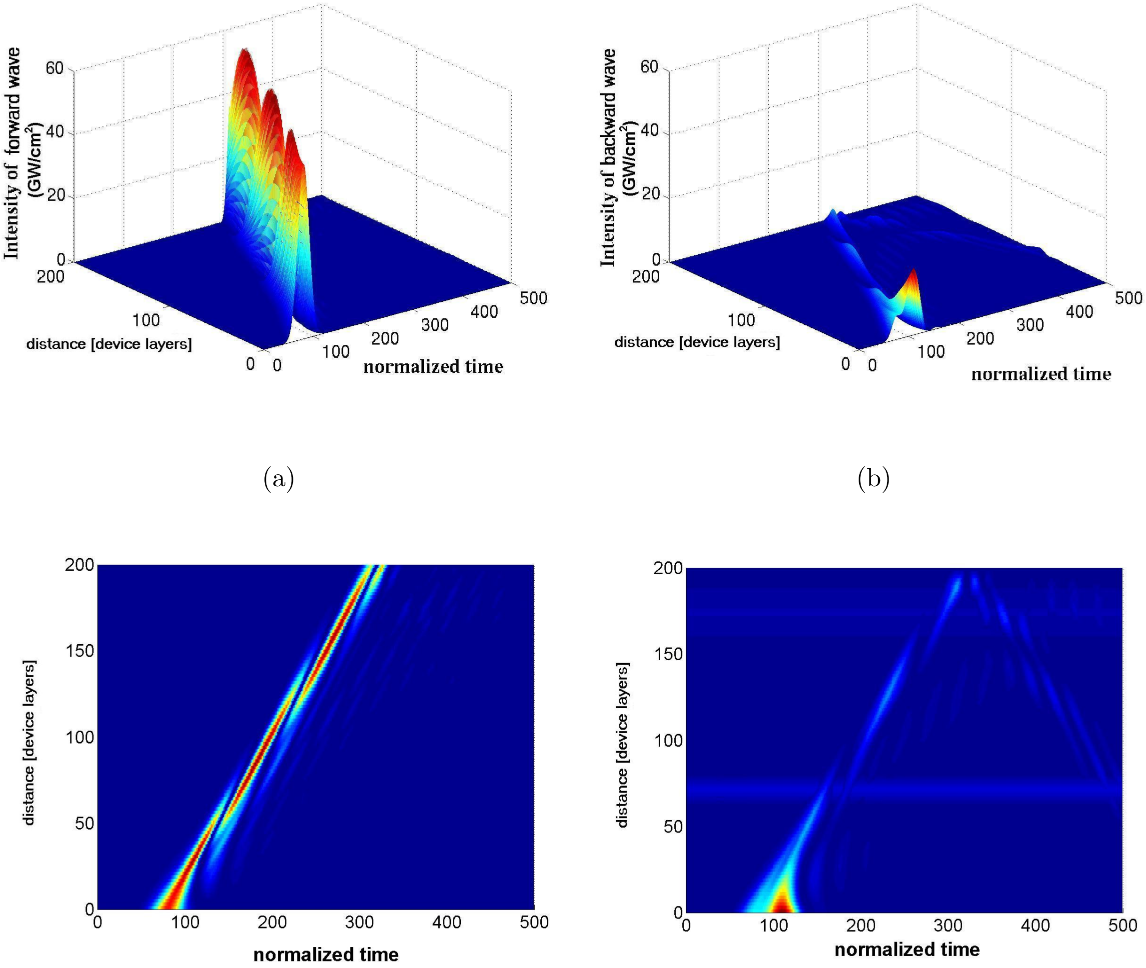

(a) (b)

(c) (d)

Figure 4.3: Gaussian pulse propagates in structure with an out-of-phase built-in linear grating ($n_{0k} = -0.1$). Compression–decompression cycling is observed. All other parameters are the same as in Figure 4.2. Shown are (a) the intensity of the forward wave, (b) the intensity of the backward wave, (c) top view of (a), and (d) top view of (b).

4.6 Summary

In this chapter, the model of pulse propagation inside a nonlinear periodic medium was further elaborated. Specifically, the range of realistic physical material parameters was defined; a numerical algorithm was described; and the two were combined to produce preliminary results for solitonic and non-solitonic pulse propagation. The analytical model of Chapter 3, together with the numerical methods and physical parameters of Chapter 4, form the basis for the explorations of nonlinear pulse propagation presented in Chapter 5.

Chapter 5

Numerical Analysis and Discussion

5.1 Introduction

Optical limiting was predicted from the steady-state analysis of nonlinear periodic structures with oppositely-signed Kerr coefficients [11]. What would be the temporal response of such device? What applications can such a device be utilized for? This chapter endeavors to find answers to these questions – matters of both fundamental and application-oriented interest. It describes the original numerical results obtained from the simulation model in the preceding chapter, revealing the limiting, pulse reshaping, and the S-curve transfer functions. Detailed time-domain analyses of the nonlinear pulse propagation through three different grating strengths are presented. The mechanisms which determine the behavior of the pulse as it propagates are also identified.

5.2 Three Case Studies

This chapter focuses on studying the behavior of a non-solitonic pulse (a Gaussian pulse) propagates in a stable nonlinear periodic structure. The steady-state analysis of this device [11] revealed its stable limiting characteristic where the transmitted intensity I_{tran} is independent of high incident intensity I_{in} for cw inputs, and the function $I_{tran}(I_{in})$ is an one-to-one function (i.e., one input corresponds to only one output). In the case of a perfectly balanced nonlinearity, $n_{nl} = 0$, it is proven in [11] that the grating operates in the stable limiting regime for both the in-phase ($n_{0k} \geq 0$) and out-of-phase ($n_{0k} < 0$) cases. In this chapter, three cases in the stable regime are studied with pulse inputs to explore the instantaneous temporal response of the device:

(i) no linear built-in grating ($n_{0k} = 0$) with balanced Kerr coefficients ($n_{nl} = 0$),

(ii) in-phase built-in grating ($n_{0k} > 0$) with balanced Kerr coefficients ($n_{nl} = 0$),

(iii) out-of-phase grating ($n_{0k} < 0$) with balanced Kerr coefficients ($n_{nl} = 0$).

In all three examples, the consideration of balanced Kerr coefficients implies that the average index of the grating remains fixed even as the pulse propagates through. The position of the center of the stopband therefore remains fixed, and it is the amplitude of the grating, and its relationship with the built-in linear grating amplitude, which varies.

5.3 Case (i): No Linear Grating with Balanced Nonlinearity ($n_{0k} = 0$ and $n_{nl} = 0$)

Figure 5.1 illustrates the refractive index profile of the Bragg grating structure with alternating layers of materials with identical linear refractive indices and oppositely-signed Kerr coefficients, i.e., $n_{0k} = 0$ and $n_{nl} = 0$. The steady-state analysis of this device is described in Figure 5.2, and shows the transmittance as a function of incident intensity. The inset of Figure 5.2 illustrates limiting behavior, wherein the intensity of the transmitted light is clamped, approaching asymptotically the limiting intensity as incident intensity increases. What happens when a ultrashort pulse is incident onto the device instead of a cw wave? Will the device demonstrate limiting behavior? Will the device display other interesting functionalities? The following sections will address these questions.

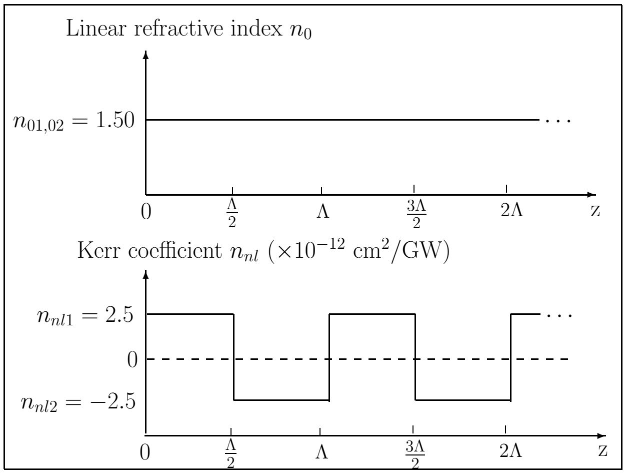

Figure 5.1: Profile of the linear refractive indices and Kerr coefficients of the device along the device length for case study (i). The refractive indices of the two adjacent layers are $n_{01} + n_{nl1}I$ and $n_{02} + n_{nl2}I$, where $n_{nl1} = -n_{nl2}$.

5.3.1 Optical Limiting

For comparison, similar device parameters as in the steady-state analysis (nonlinearity, length, and periodicity) are applied to investigate the instantaneous temporal response of the structure. Instead of the cw inputs as in the steady-state analysis, pulses which take the form of (4.12) are introduced for the following time-domain study. These pulses have a fixed transform-limited width of 605 fs with different peak intensities to give varying energies. This pulse width corresponds to a spectral bandwidth of 1.6 THz which is smaller than the maximum bandwidth of the stopband created by the nonlinear grating, i.e., $\Delta\omega \approx \frac{2}{\pi}\frac{\Delta n}{\bar{n}}\omega = 1.7$ THz. Figure 5.3 illustrates the energy transmittance as a function of incident pulse energy. The term 'energy transmittance' is defined in a similar way to the intensity transmittance in the cw case: it is the ratio of the total transmitted energy density $\mathcal{W}_{tran}$ to the total incident pulse energy density $\mathcal{W}_{in}$, where the energy densities are defined in Eq. (4.11). The peak intensities of the transmitted pulses are also recorded, and plotted in the inset of Figure 5.3. The limiting behavior demonstrated in this figure closely resembles the steady-state response reported in Figure 5.2. The limiting effect

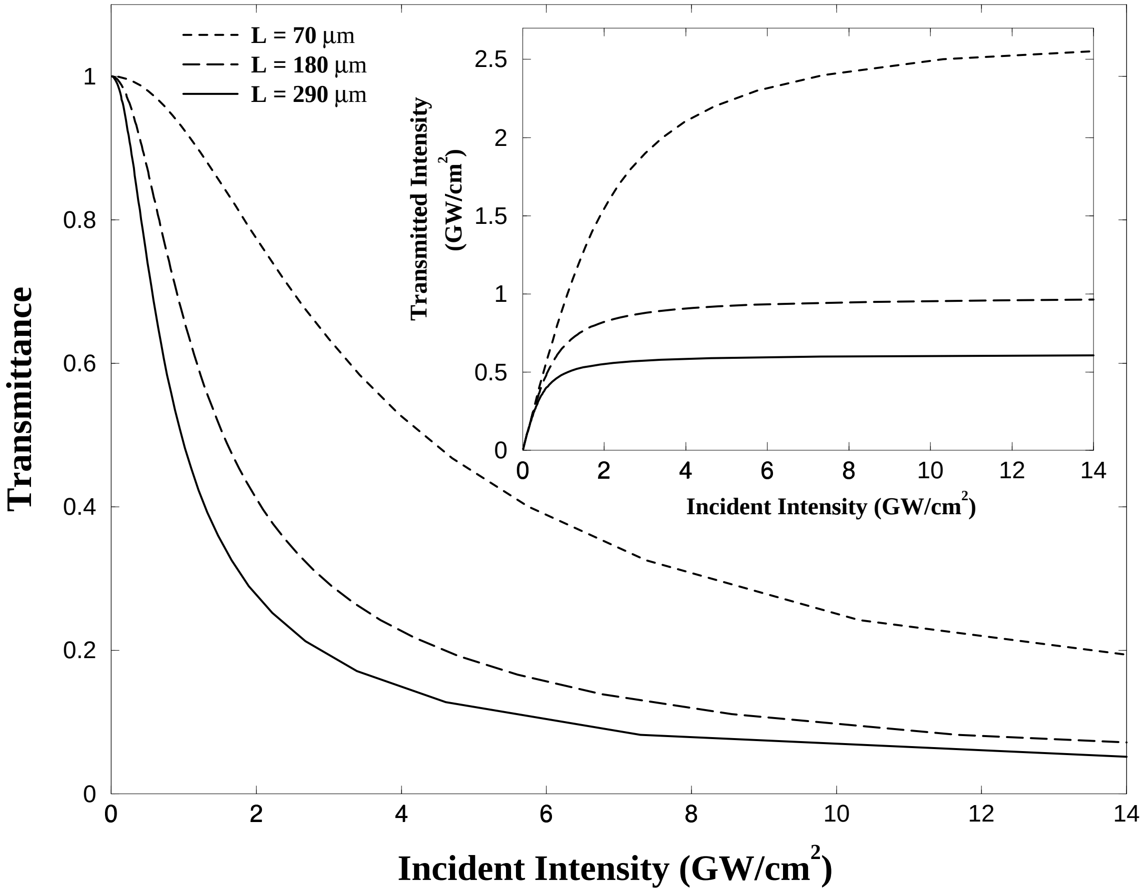

Figure 5.2: Steady state analysis: Transmittance as a function of incident intensity for various device lengths: L = 70 μm, 180 μm and 290 μm. Inset: transmitted intensity level versus incident intensity for the same device, demonstrating characteristic limiting behavior.

is less pronounced for energy. However, in contradistinction with steady-state average power results, the time-domain transmitted energy is not asymptotically limited. For very low incident peak intensities the refractive indices of the two adjacent layers are matched. Thus the device is transparent to the incoming light, resulting in a close-to-unity transmittance. Increasing the intensity causes the indices to change, which creates a grating, leading to reflection. As the peak intensity of the incident pulse increases further, the peak intensity of the transmitted pulse eventually approaches a limiting intensity. Figure 5.3 also illustrates the decreasing limiting intensity with increasing

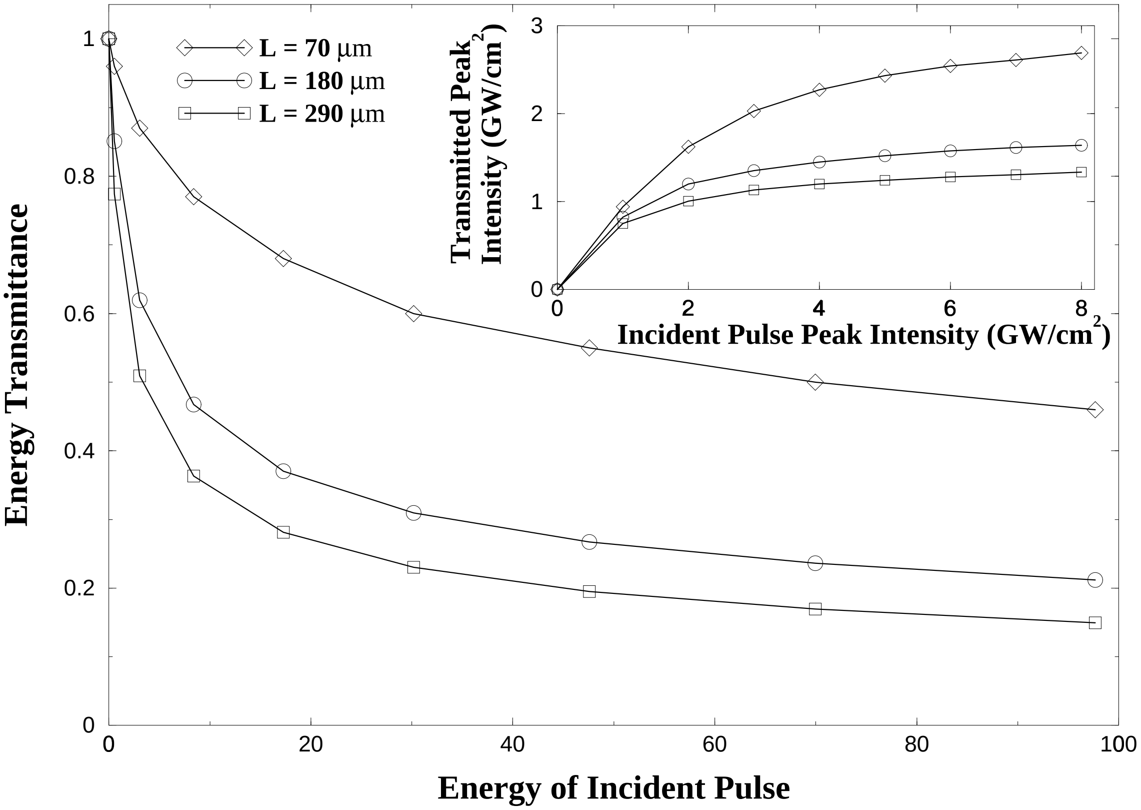

Figure 5.3: Time-domain analysis: Energy transmittance as a function of incident pulse energy. Inset: peak intensity of the transmitted pulse versus peak intensity of the incident pulse. Incident pulses with a fixed width of 605 fs and varying peak intensities are introduced to the device with length L = 70 μm, 180 μm and 290 μm.

number of periods (longer devices). The transmitted peak intensity of a 605 fs pulse is shown to be limited roughly at 1.2, 1.6, and 2.8 GW/cm^2 for a 290, 180, and 70 μm-long device, respectively.

The results presented in Figure 5.3 are for fixed incident pulse width. In contrast, Figure 5.4 illustrates the energy transmittance as a function of pulse width, given that the incident peak intensity remains constant. In these numerical computations, the incident pulse again takes the form of (4.12) with a fixed peak pulse intensity of $I_{peak} = 4$ GW/cm^2, such that the maximum magnitude of change in the refractive index is equal to the chosen 0.01. The graph displays the limiting behavior of the pulse transmission and the

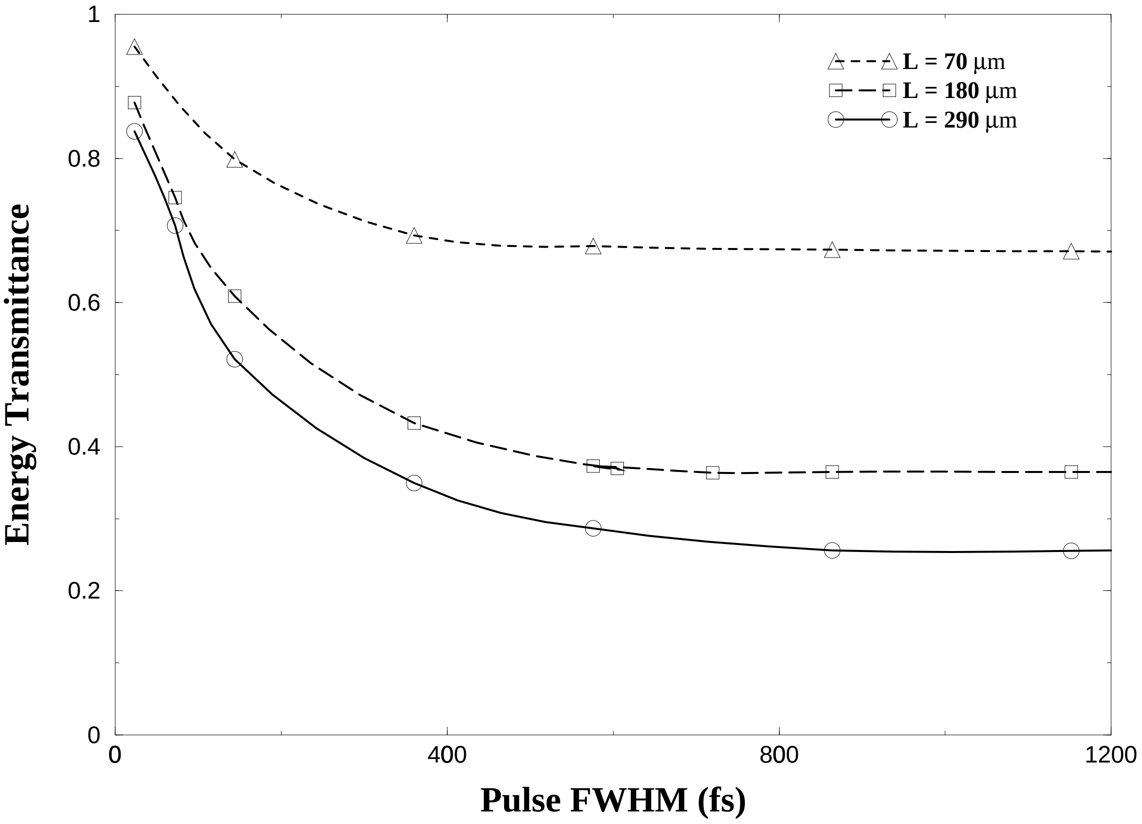

Figure 5.4: Time-domain analysis: Pulse transmittance as a function of pulse width for a fixed peak pulse intensity of $I_{peak} = 4$ GW/cm^2 for device lengths of L = 70 μm, 180 μm and 290 μm. The transmittance of the device drops to a limiting value in each case.

bandwidth dependence of the transmission.

Long-duration pulses in Figure 5.4 exhibit the desired limiting behavior because their spectral bandwidth lies entirely inside the stopband of the grating, leading to bandwidth-independent transmittance. Short-duration pulses, on the other hand, have a spectral bandwidth which exceeds the width of the dynamic stopband, resulting in transmission of the portion of the power which lies outside of the stopband of the device. In the limit of short pulse duration, the pulse bandwidth is wide enough that most of its power lies outside the nonlinear stopband; hence the pulse transmittance approaches unity. The knee in the characteristic of Figure 5.4 occurs when the pulse bandwidth and nonlinear stopband bandwidth become comparable:

$$\Delta\omega_{gap} = \frac{4(n_{nl1} - n_{nl2})I_{peak}}{\pi(n_{01} - n_{02})}\omega_0 \tag{5.1}$$

In Figure 5.4, the transmittance decreases from 0.75 to 0.25 when the device length is increased from 70 μm to 290 μm. The pulse intensity decays as the pulse evanesces along the length of the device.

We now consider the case of pulses of fixed energy, where the intensity and temporal width are co-varied to satisfy this constraint. The spectral bandwidth (1/FWHM) increases with the same proportionality as the bandwidth of the grating ($\Delta n \propto n_2 I_{peak}$). If a given pulse has a peak intensity, bandwidth, and $n_2 I_{peak}$ combination such that the pulse bandwidth lies within the nonlinear grating bandwidth, then it will continue to do so when a second pulse of the same energy with narrower temporal width and higher in peak intensity.

In summary, an optical limiter may be designed which will guarantee that its output peak intensity will be less than a required intensity. This is achieved through the choice of the number of layers, peak intensity, and temporal width. It is observed that the time-domain transmitted energy is not asymptotically limited as in the steady-state case. It is also noted that the limiter does not require large number of layers. For instance, the transmitted peak intensities of a 605 fs incident pulse (with a characteristic length of 180 μm) are less than 1.2, 1.6, 2.8 GW/cm^2 for a device length of 290 μm, 180 μm and 70 μm, respectively.

5.3.2 Pulse Shaping

In Section 4.5, Figure 4.2 illustrated the non-solitonic character of Gaussian pulse propagation through a balanced nonlinear structure with constant linear indices ($n_{0k} = 0$ and $n_{nl} = 0$). Both the amplitude and the shape of the Gaussian pulse were distorted. The shape of the transmitted pulse depended on the size of the structure and the initial pulse width. Figure 5.5 shows the transmitted pulse shapes through a 180 μm-long device for two different temporal widths. The input Gaussian pulses are 605 fs wide in Figure 5.5(a) and 1440 fs wide in Figure 5.5(b), and both have a 4 GW/cm^2 peak intensity.

The bandwidth of both pulses is much less than the effective bandwidth of the device, allowing us to focus attention on intensity self-patterning of the pulses and to remove the effects of incomplete spectral blocking. To explain the distortion in the transmitted pulses, the time-dependent transmittance of the induced nonlinear grating is calculated, and illustrated in Figure 5.6(a) and 5.6(b). For the shorter pulse length of 180 μm, Figure 5.6(a) shows that the forward- and backward-propagating waves form their strongest instantaneous gratings at different times. The backward-propagating wave gives rise to an additional delayed replica of the transmitted pulse in the time-dependent transmittance, causing the dip in the transmitted pulse of Figure 5.5(a). When the incident pulse is longer than the device (435 μm in this example), the strongest instantaneous gratings are formed roughly at the same time for forward- and backward-propagating waves (Figure 5.6(b)). Sequential multiple reflections of pulses inside the relatively short structure create echoed patterning of the transmitted pulse seen in Figure 5.5(b).

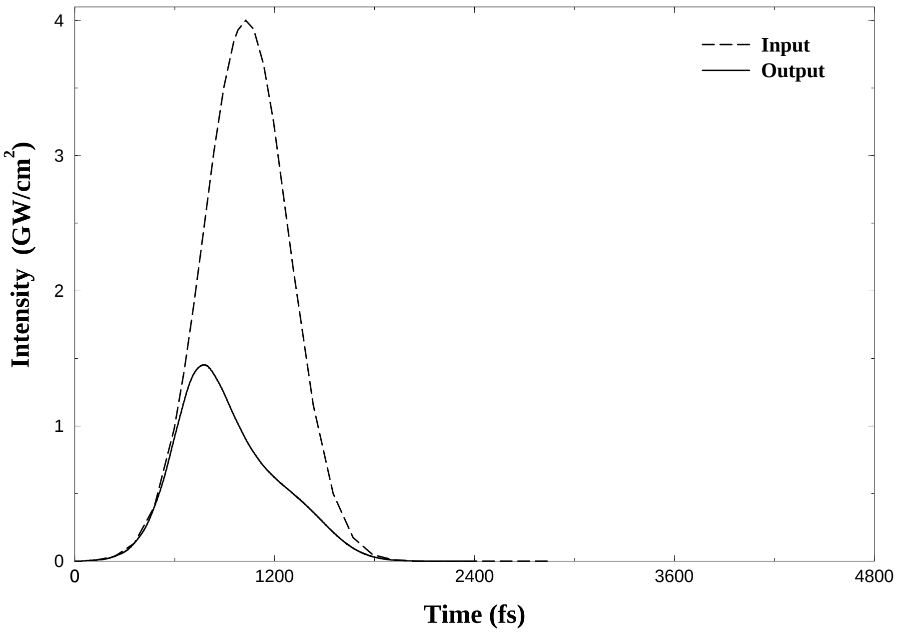

(a)

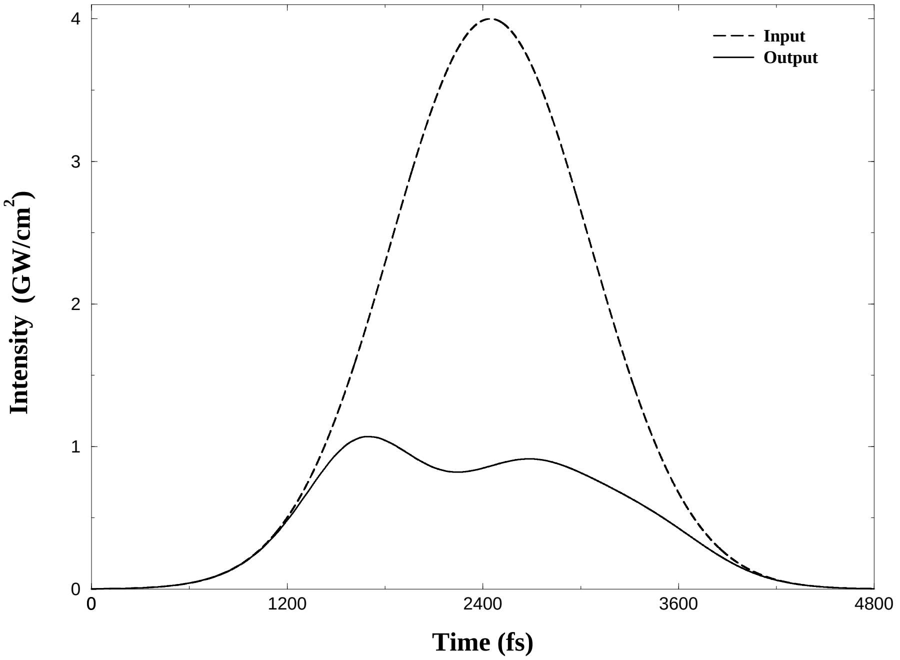

(b)

Figure 5.5: Input and output intensities of a pulse propagating through a 180 μm-long device for an input pulse width of: (a) 605 fs or characteristic length of 180 μm and (b) 1440 fs or characteristic length of 435 μm.

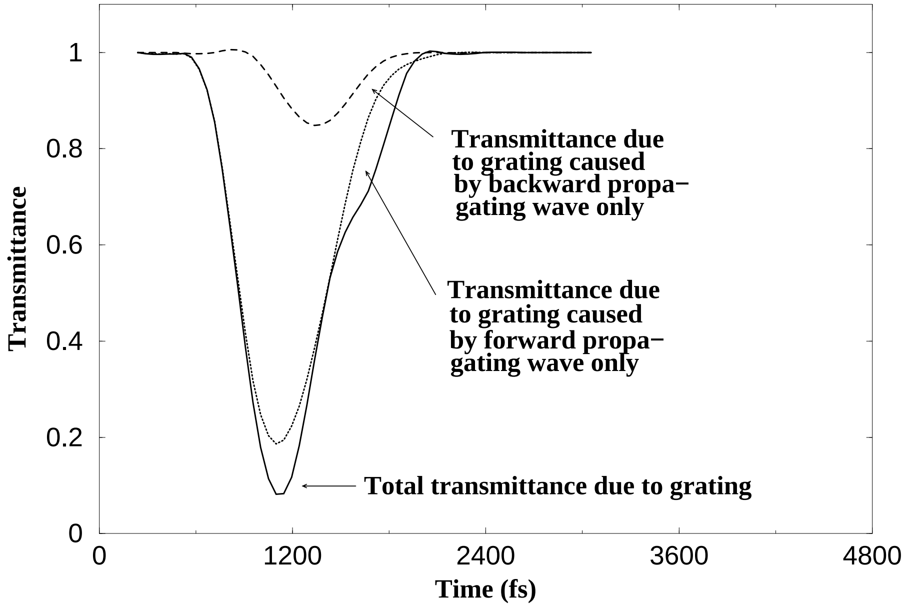

(a)

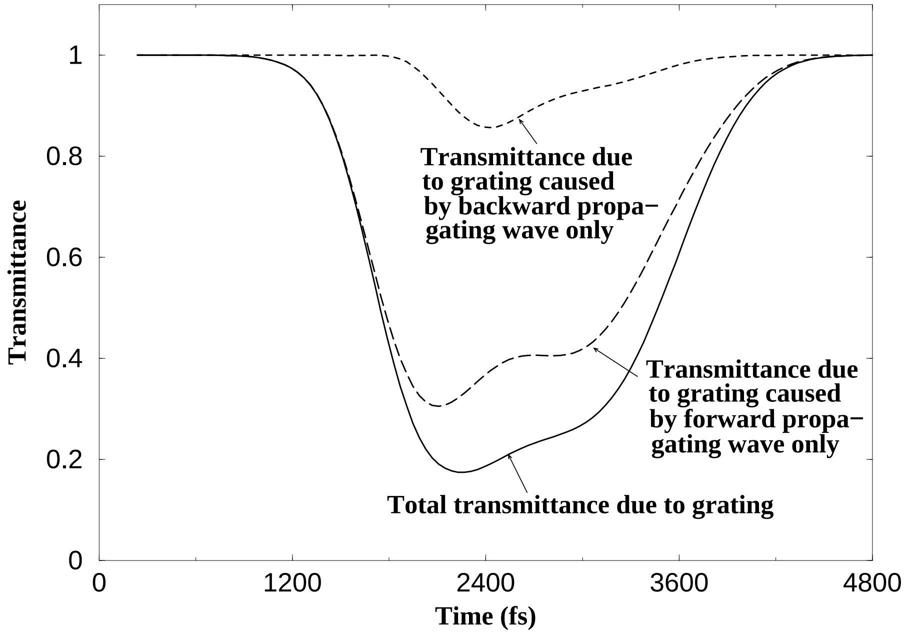

(b)

Figure 5.6: Heuristic analysis of pulse shaping in a 180 μm-long nonlinear grating. The time dependent instantaneous transmittance attributable to contributions from forward- and backward-propagating pulses for an input pulse width of: (a) 605 fs or characteristic length of 180 μm and (b) 1440 fs or characteristic length of 435 μm.

5.4 Case (ii): In-phase Built-in Linear Grating with Balanced Nonlinearity ($n_{0k} > 0$ and $n_{nl} = 0$)

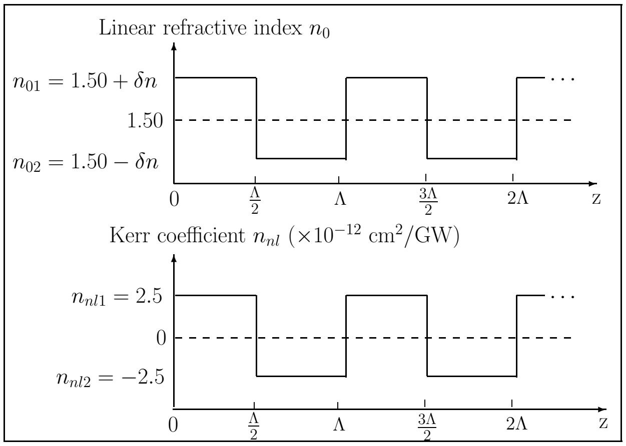

Figure 5.7: Profile of the linear refractive indices and Kerr coefficients of the device along the device length for case study (ii). The refractive indices of the two adjacent layers are $n_{01} + n_{nl1}I$ and $n_{02} + n_{nl2}I$, where $n_{nl1} = -n_{nl2}$.

We now consider periodic structures with an in-phase linear built-in grating such that $n_{0k} > 0$ and $n_{2k} > 0$, as illustrated in Figure 5.7. The intensity-induced nonlinear grating adds constructively to the existing built-in linear grating, resulting in low transmittance. No significant transmitted pulse energy is observed for a large range of different input pulses, since most of the incident light is blocked by the linear built-in grating. This is evident in the bottom curve of Figure 5.9(a), constructed for the in-phase linear grating with $n_{0k} = 0.01$, i.e. $n_{1,2} = (1.50 \pm 0.01) \pm (2.5 \times 10^{-12} \text{ GW/cm}^2)I_{in}$.

5.5 Case (iii): Out-of-phase Built-in Linear Grating with Balanced Nonlinearity ($n_{0k} < 0$ and $n_{nl} = 0$)

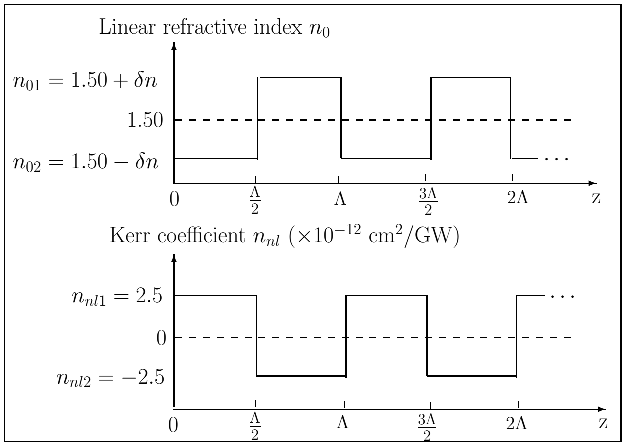

Figure 5.8: Profile of the linear refractive indices and Kerr coefficients of the device along the device length for case study (iii). The refractive indices of the two adjacent layers are $n_{01} + n_{nl1}I$ and $n_{02} + n_{nl2}I$, where $n_{nl1} = -n_{nl2}$.

Here periodic structures with an out-of-phase linear built-in grating are considered, such that $n_{0k} < 0$ and $n_{2k} > 0$, as shown in Figure 5.8. The out-of-phase linear built-in grating allows for a dynamic balance with the intensity-induced nonlinear grating as the pulse propagates through the structure. When the intensity of the pulse exceeds that required to take the instantaneous nonlinear grating through the zero point and over to the other sign, the grating is bleached and then re-established as the incident pulse propagates through the structure.

5.5.1 *S*-curve and *N*-curve Transfer Characteristics

We begin by investigating the effects of grating strength on the transmittance of the device. In this analysis, a fixed incident pulse with width of 605 fs is launched at structures with linear out-of-phase gratings of $n_{0k} = -0.002$, $n_{0k} = -0.005$, and $n_{0k} = -0.01$. The intensity $I_{cl} = |n_{0k}|/n_{2k}$ which causes the nonlinear index change to balance completely with the out-of-phase linear grating, is referred to as the *closing intensity*. When the balance between linear and nonlinear grating closes the overall grating profile, the device is locally transparent. The total transmitted pulse energy density versus the total incident pulse energy density is shown in Figure 5.9(a) for the out-of-phase linear gratings listed above. The pulse energy transmittance is shown in Figure 5.9(b) for the same out-of-phase linear gratings.

When the out-of-phase linear grating is large enough to effect a significant built-in reflectance (for example, when the built-in linear index difference is 0.01), the transmittance reveals an interplay between built-in and intensity-dependent grating behavior. At small incident pulse intensities the linear built-in grating blocks most of the light, resulting in a close-to-zero transmittance. The transmittance gradually increases as the increasing intensity-induced nonlinear index change offsets the linear grating. The closing and reopening of the grating are responsible for the S-curve character of the transfer function in Figure 5.9(a), which may be used for optical logic gates such as an AND gate [31, 38]. The energy transmittance is at its maximum when the peak intensity of the incident pulse is at the closing intensity. Here the regions around the peak of the pulse bleach out the grating.

Long-duration pulses exhibit the limiting trend of Figure 5.9(b). However, the energy transmittance of linear built-in gratings does not converge to the case of constant linear index across the device: the more intense are the input pulses, the more there exist regions where the self-induced nonlinear grating matches with the built-in linear grating, and the transmittance is higher than that with no linear grating.

Since the energy transmittance displays an interesting S-curve character for a grating strength of 0.01, this grating strength becomes the focus of the study. The transfer characteristics of the peak intensities are plotted in Figure 5.10. Unlike the one-step limiting characteristics as shown in the inset of Figure 5.3, the peak intensities of the

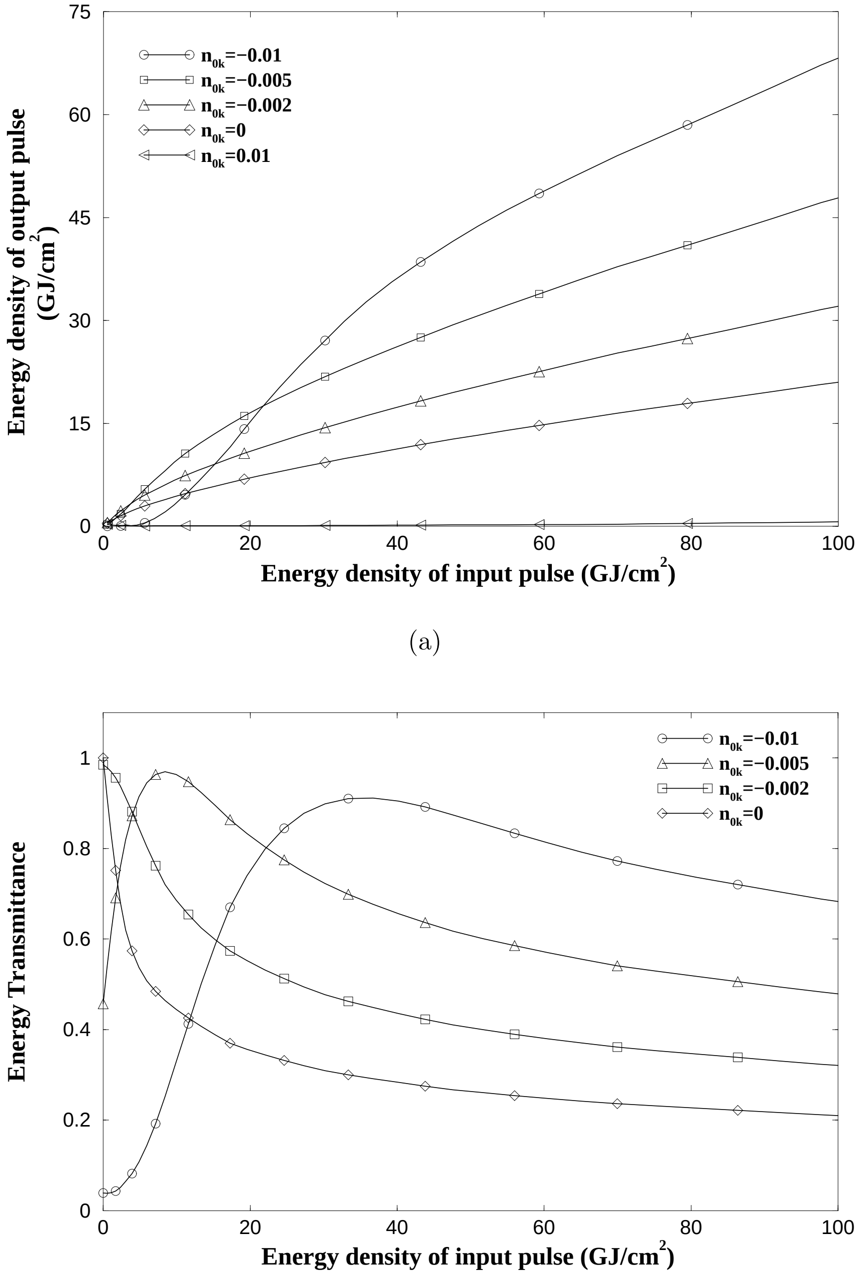

(a)

(b)

Figure 5.9: (a) Total pulse transmitted energy density versus total incident pulse energy density for linear in- and out-of-phase built-in gratings; (b) Corresponding energy transmittance as a function of incident pulse energy. A pulse width of 605 fs and a device length of 180 μm were fixed for all cases.

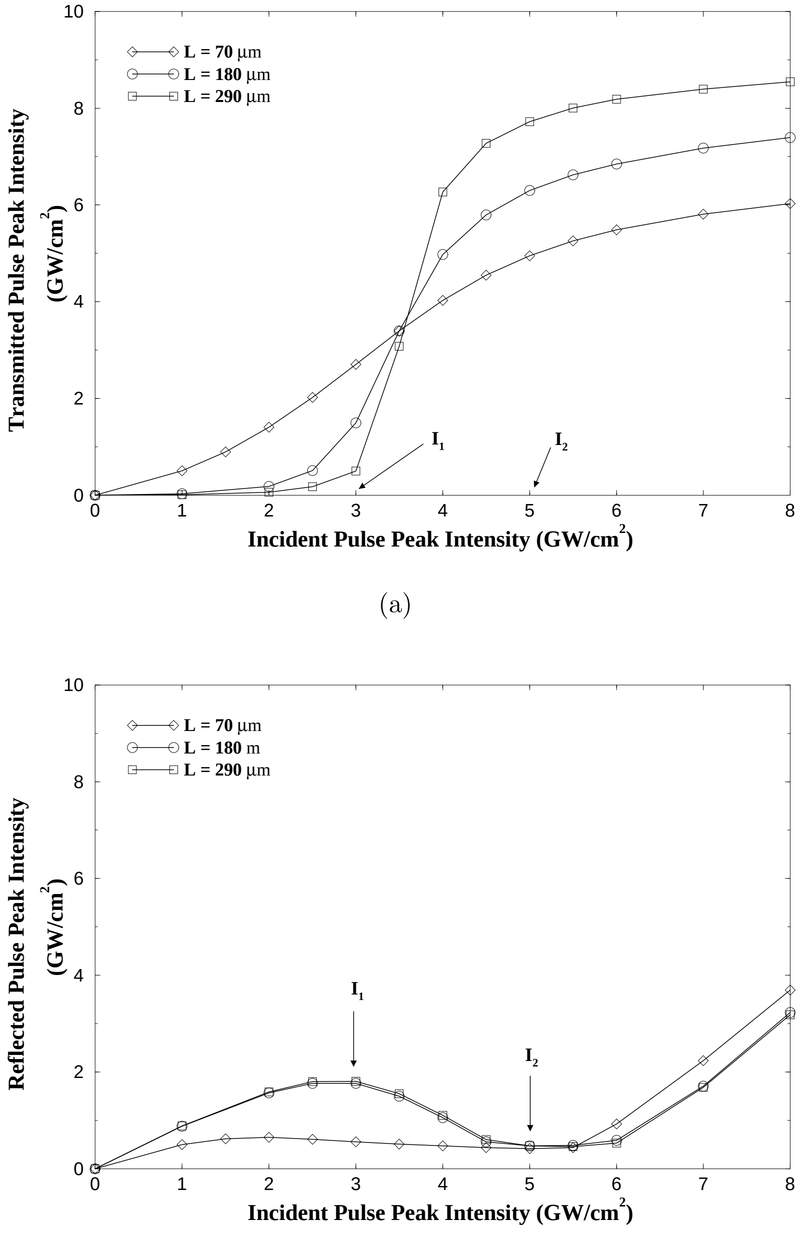

(a)

(b)

Figure 5.10: Transfer characteristics of pulse peak intensities for varying device lengths: (a) S-curve for the peak intensities of the transmitted pulses; (b) N-curve for the peak intensities of the reflected pulses. I_1 and I_2 are two threshold intensities. Incident pulses with a fixed width of 605 fs propagate through device length of 70 μm, 180 μm, and 290 μm. The device has a 0.01 out-of-phase linear grating.

transmitted and reflected pulses exhibit an S- (Figure 5.10(a)) and an N-curve character (Figure 5.10(b)), respectively. These characteristics are more obvious for longer devices.

The S- and N-curve transfer characteristics can enable a complete logic set [31]. We consider the curve with the device length $L = 290$ μm, for example: an incident pulse which is combined by 2 input pulses from a 3 dB coupler propagates through the nonlinear periodic structure with the S-curve transfer character. If a logic 1 is assigned to the peak intensity corresponding to $I \geq I_2$ in Figure 5.10(a) and a logic 0 is assigned to the peak intensities corresponding to $I \leq I_1$, an output will only be observed when both input pulses are present, i.e. $I_{in1}, I_{in2} \geq I_2$. This is an AND operation.

In summary, optical logic gates may be formed using a nonlinear periodic structure with a linear built-in grating. The longer the device, the better the functionalities. S- and N-curve transfer characteristics required for optical logic gates are observed.

5.5.2 Pulse Compression

We now proceed to examine the influence of device length on transmitted pulse shapes in the presence of an out-of-phase linear grating with $n_{0k} = -0.01$. The peak intensity of the incident pulse is fixed to $I_{peak} = 4$ GW/cm^2 to close the grating, and the pulse width is fixed at $FWHM = 605$ fs. The initial stage of the pulse compression, reshaping and high-amplitude multiple-peak oscillation effects are shown in Figure 5.11 for different device lengths. A maximum of 88% pulse compression is observed for a 720 μm-long device. This process resembles Gaussian pulse propagation in the out-of-phase linear gratings displayed in Figure 4.3. Figure 4.3 and Figure 5.11 differ only in the parameters used for the incident pulse. For a smaller peak intensity I_{peak} and larger pulse width, the pulse reshaping and multiple-peak oscillations in Figure 5.11 occur further into the device as compared to those in Figure 4.3. For this reason we study in detail the initial stage of pulse compression for $L < 300$ μm, when the compressed Gaussian pulse preserves a single-peak shape.

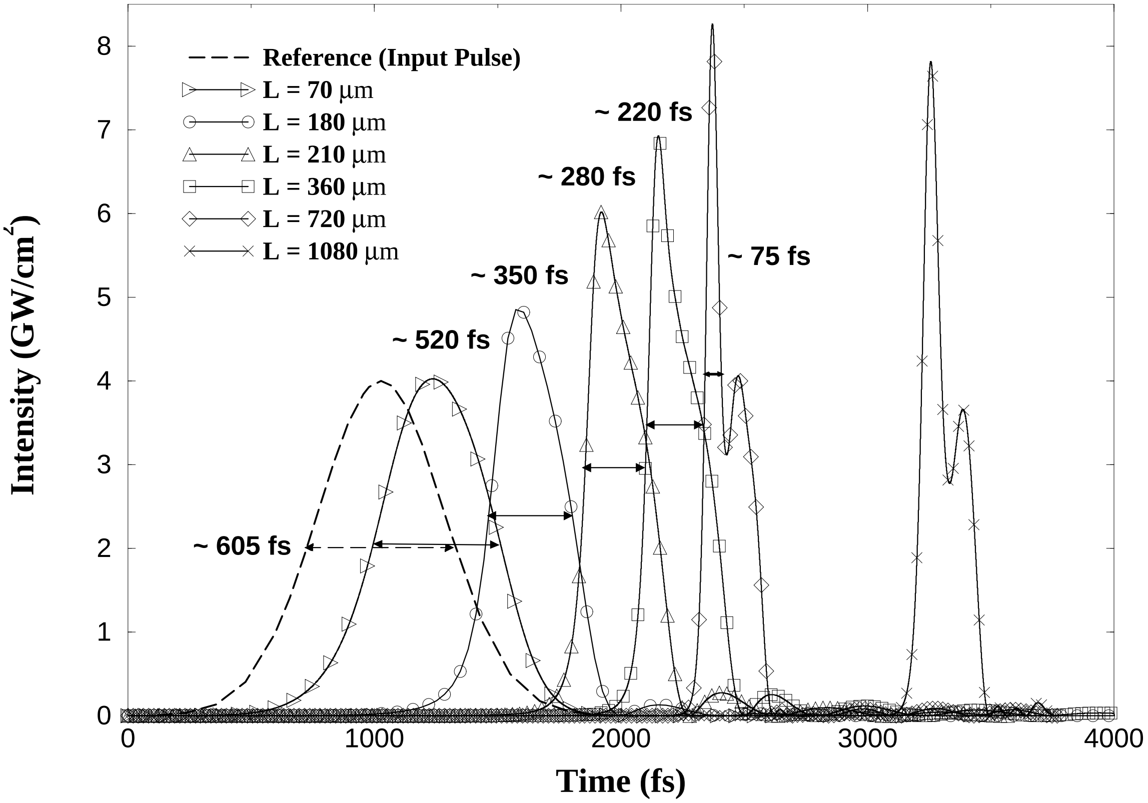

Figure 5.11: Output temporal response of the device with length L = 70 μm, 180 μm, 290 μm, 360 μm, 720 μm, and 1080 μm for a fixed input pulse with $I_{peak} = 4$ GW/cm^2 and $FWHM = 605$ fs. Pulse compression, reshaping, and double-peak oscillations are observed.

It can be proven analytically that pulse compression can result from an out-of-phase built-in linear grating, assuming the incident pulse takes the form of (Eq. 4.12). For $n_{nl} = 0$, zero initial conditions, and a real boundary value of $A_+(0,T) = \sqrt{I_{in}(T)}$, the coupled-mode system (3.19)–(3.20) can be simplified to

$$A_+ = u(Z,T), \quad A_- = iy(Z,T),$$

where u and y are real variables satisfying the system:

$$\frac{\partial u}{\partial Z} + \frac{\partial u}{\partial T} = -\left[n_{0k} + n_{2k}\left(u^2 + y^2\right)\right] y, \tag{5.2}$$

$$\frac{\partial y}{\partial Z} - \frac{\partial y}{\partial T} = -\left[n_{0k} + n_{2k}\left(u^2 + y^2\right)\right] u. \tag{5.3}$$

It follows from Eq. (5.3) if $n_{0k} < 0$ that the time-derivative $\partial y/\partial T$ is negative for $y \approx 0$ and $0 < u(T) < \sqrt{I_{cl}}$. Here $I_{cl} = |n_{0k}|/n_{2k}$ is the closing intensity. Therefore, when the Gaussian pulse (Eq. 4.12) enters the device at the input $Z = 0$, the generated backward wave field y is always negative. The other equation (5.2) defines the rate of change of the pulse amplitude in the reference frame moving to the right with unit speed (the speed of the Gaussian pulse). At the peak of the Gaussian pulse, the rate of change is positive if $y < 0$ and $I_{peak} > I_{cl}$. Therefore, the Gaussian pulse with peak intensity I_{peak} exceeding the closing intensity I_{cl} is compressed in width and increased in peak amplitude by the out-of-phase built-in linear grating. On the other hand, similar analysis shows that the Gaussian pulse with $I_{peak} < I_{cl}$, or the Gaussian pulse in the in-phase built-in linear gratings with $n_{0k} \geq 0$, is decompressed in width and decreased in amplitude during propagation in the nonlinear periodic structure.

To validate and explain the observation of pulse compression, we seek to reveal the evolution of the pulse, and consequently the instantaneous grating, in time and space across the device. Figure 5.12(a) shows the rate of change in amplitude of the forward propagating wave, or $\left(\frac{\partial A_+}{\partial T} + \frac{\partial A_+}{\partial Z}\right)$, in a 180 μm-long device. As follows from Eq. (5.2), the forward-propagating wave is enhanced when the backward-propagating wave is coupled in. Moreover, the rate of change in amplitude of $A_+(Z,T)$, or $\left(\frac{\partial A_+}{\partial T} + \frac{\partial A_+}{\partial Z}\right)$, resembles the profile of the backward propagating envelope $A_-(Z,T)$. The M-shaped graph along the time axis describes the existence of pulse propagation along the device length.

Figure 5.12(b) provides insight into the mechanism of pulse compression. In Figure 5.12(c) we compare a reference input pulse to a compressed pulse. The slopes of the amplitude of the compressed envelope is smaller than that of the reference Gaussian pulse at the beginning stages of a compressing process (up to time $t = a$). The slopes of the compressed pulse then increases dramatically before reaching the peak. The slopes of the compressed pulse is bigger than that of the reference pulse at the range time $c < t < b$.

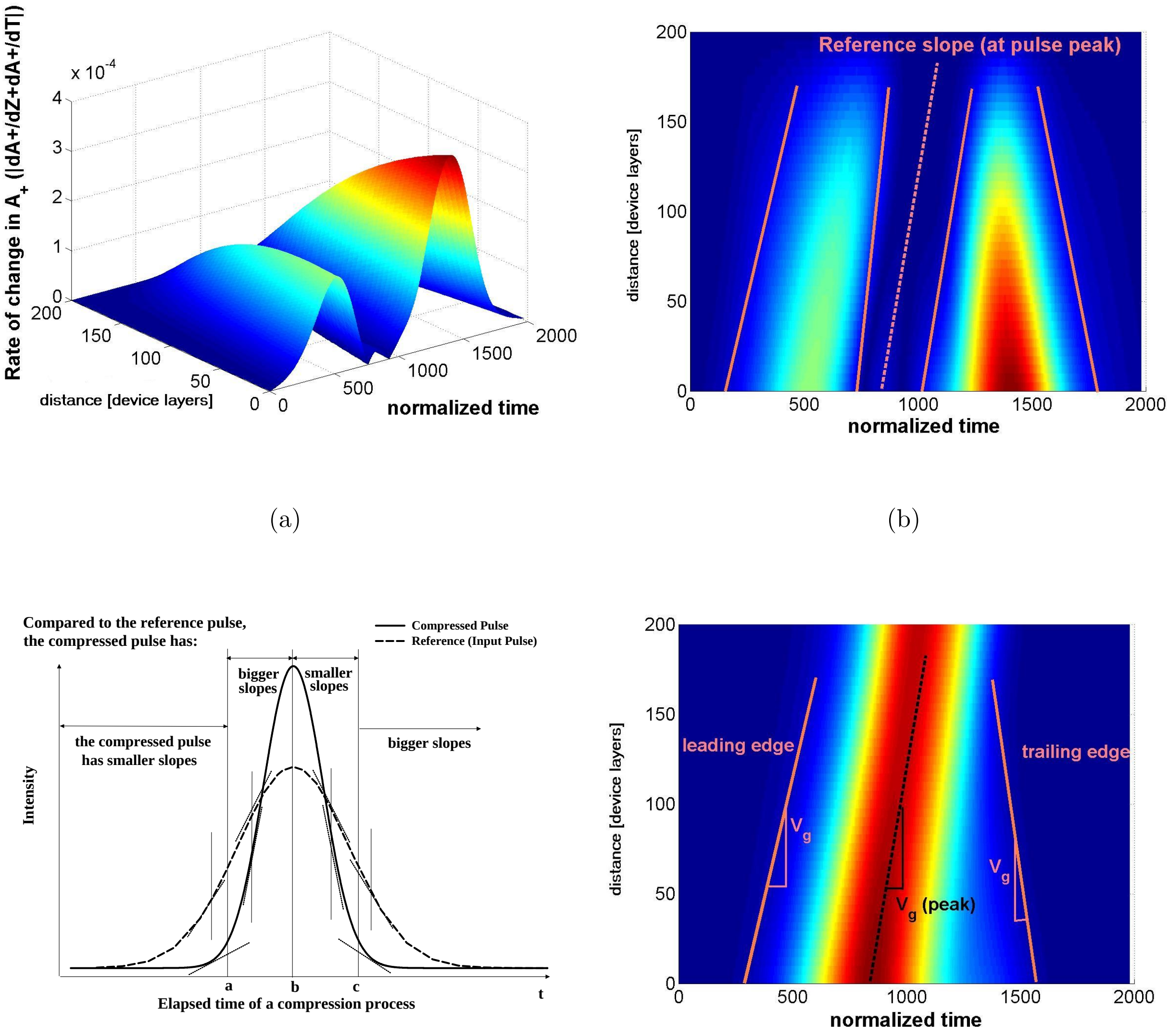

(a) (b)

(c) (d)

Figure 5.12: (a) Rate of change in amplitude of the forward propagating wave; (b) top view of (a); (c) a simplified intensity diagram of an incident pulse and a compressed pulse; (d) a plot of the intensity of the propagating wave in time and space. A pulse with $I_{peak} = 4$ GW/cm^2 and $FWHM = 605$ fs is launched into the input of a 180 μm-long device.

Similar arguments apply to the second half of the compressed pulse, except the slopes of the compressed envelope are smaller compared to the reference pulse at time $b < t < c$, and bigger after $t = c$ at the final stages of the compressing process. The convergence of the four slopes of the M-shape along the device length in Figure 5.12(b) shown by the four orange solid lines implies pulse compression.

As the pulse propagates through the structure, the intensity-induced nonlinear grating gradually offsets the existing linear built-in grating, reaching a 0 total grating. The sum of forward- and backward-propagating intensities can give rise to an instantaneous peak intensity which exceeds that required to close the grating completely at some time instances. For a short period of time the nonlinear grating dominates the index grating, which creates a slight in-phase total grating (positive values). Figure 5.12(d) depicts this process in a 500-layer (180 μm long) device. The front of the pulse travels approximately at the same speed as the peak of the pulse. The trailing edge, however, catches up with the leading edge, resulting in pulse compression. The effect resembles the pushbroom effect described in both [6] and [7]. Here, however, instead of using both pump signal and probe beam, only one strong pulse is used to alter the local refractive index of the medium – resulting in a self-induced pushbroom effect.

The compression effects are observed when the peak pulse intensity I_{peak} is set to close completely the grating, i.e. $I_{peak} = I_{cl} = |n_{0k}|/n_{2k}$. If the intensity-induced nonlinear grating is small compared to the out-of-phase linear grating, the transmittance is expected to be lower due to reflection by the grating. A pulse (give by Eq. 4.12) with peak intensity $I_{peak} = 2$ GW/cm^2 chosen to give a maximum nonlinear grating of 0.005 (lower than the out-of-phase linear built-in grating $n_{0k} = -0.01$) is simulated. In the case of a higher input peak intensity I_{peak}, the nonlinear grating will dominate the grating profile, resulting in a switching of the sign of the grating profile. Similar to the $I_{peak} = 4$ GW/cm^2 case, the energy of forward- and backward- propagating waves will be stored inside the grating, causing pulse compression during transmission. Figure 5.13(b) shows the compressed output pulse simulated when the peak incident pulse is $I_{peak} = 6$ GW/cm^2 which provides a maximum induced nonlinear grating of 0.015 (higher than the out-of-phase linear grating $n_{0k} = -0.01$).

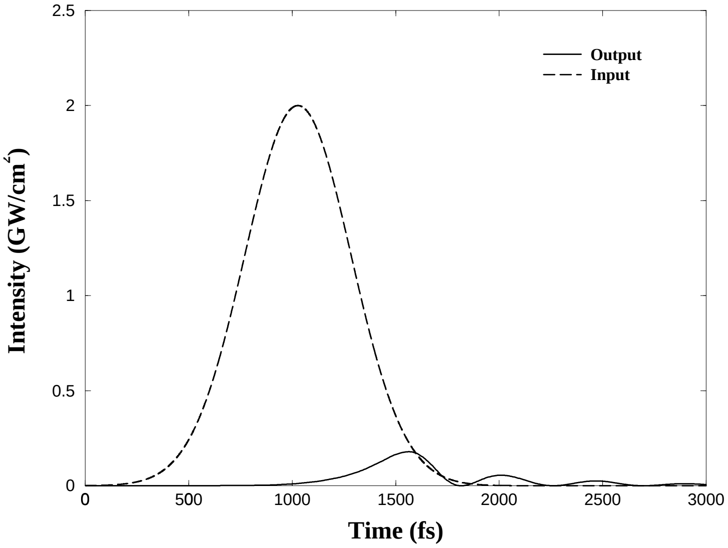

(a)

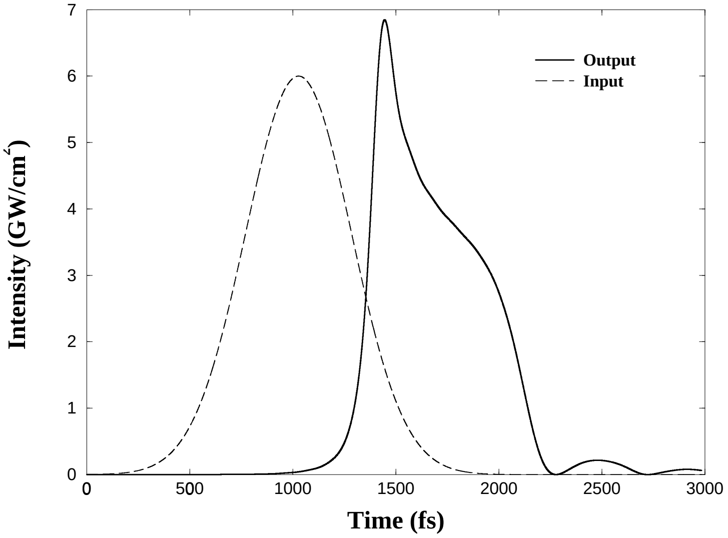

(b)

Figure 5.13: Transmitted pulse (output) shapes when the intensity of the incident Gaussian pulse is set to: (a) $I_{peak} = 2$ GW/cm^2 and (b) $I_{peak} = 6$ GW/cm^2. The width of the pulse is $FWHM = 605$ fs and the device length is fixed to $L = 180$ μm.

Summarizing, envelope compression in nonlinear optical structures with an out-of-phase built-in linear grating is observed when the device length does not exceed twice the input pulse width and the peak input intensity meets or exceeds that required to close the grating.

5.6 Summary

This chapter presented the results obtained from the simulations and performed a numerical analysis to investigate pulse propagation behavior in a nonlinear Bragg structure. Three cases of grating strength (i.e., no built-in grating, in-phase built-in grating, and out-of-phase grating) were examined. In the absence of the linear grating, the energy transmittance of pulses with small bandwidth (compared to the bandwidth of the grating) was independent of pulse width. The limiting behavior of the device was pulse-bandwidth-dependent. The mechanisms behind output pulse shape formation for long-duration pulses were distinguished from that for short-duration pulses. In the presence of the out-of-phase linear grating, S-curve transfer characteristics were observed due to the erasure and reopening of the stopband. A compression effect reminiscent of the pump-probe pushbroom effect for a single pulse was predicted and a mathematical proof for pulse compression was also provided.

The temporal analysis of the pulse propagation presented in this chapter explored the limiting, logic operations, and pulse reshaping functions of the nonlinear Bragg structure. An optical limiter was demonstrated to limit the transmitted peak intensity of a 605 fs pulse to 1.2, 1.6, and 2.8 GW/cm^2 for a 290, 180, and 70 μm-long device, respectively. A 0.01 out-of-phase linear grating with a length of at least 180 μm was observed to have an S- and an N-curve transfer characteristic. A 720 μm-long device with the same out-of-phase grating was shown to exhibit significant pulse compression, compressing a pulse to 12% of its original pulse width.

Chapter 6

Conclusions

6.1 Thesis Overview

In present-day networks, most of the complex signal-processing operations such as switching, logic functions, or routing are performed in the electrical domain. This necessitates costly electro-optical (EO) and opto-electrical (OE) conversions. The intent of this work was to investigate the suitability of a nonlinear Bragg structure with alternating oppositely-signed Kerr coefficients for high-speed all-optical time-domain signal processing. Such a device would reduce the need for repeated EO and OE conversions.

Chapter 2 discussed the basic concepts of Bragg gratings and nonlinearity in order to establish a understanding of the topic of nonlinear periodic structures. Previous research on this topic was reviewed. Although many different nonlinear periodic structures have been studied in the past, one important class of stable devices, those with alternating layers of nonlinear materials with balanced Kerr coefficients, had been neglected. It was therefore proposed to study the temporal response of such stable devices.

Chapter 3 derived a system of coupled-mode equations which captures the physical mechanisms of this class of stable nonlinear periodic devices. Under special circumstances, a Bragg soliton may propagate. The exact solutions for a Bragg soliton were solved from the coupled-mode system in this chapter.

The analytical framework described in Chapter 3 was necessary in developing a convergent numerical solution of the equations. In Chapter 4, the implementation of this simulation model was presented. The boundary conditions were stated and the device parameters were defined and justified according to the experimental literature for nonlinear materials properties. Simulations of Bragg soliton and non-solitonic pulse propagation were presented to validate the method of numerical solution.

Chapter 5 presented three sets of numerical analyses of nonlinear pulse propagation through three different grating strengths: no built-in linear grating, in-phase linear grating, and out-of-phase linear grating. The pulse propagation in each case was described and the mechanisms which determine the behavior of the pulses were identified. In the absence of the linear grating, the limiting behavior of the device was concluded to be pulse-bandwidth-dependent. Here, the mechanisms behind pulse shape formation for long-duration pulses were distinguished from those for short-duration pulses. In the presence of the out-of-phase linear grating, S-curve transfer characteristics were predicted and explored. The simulation results were also used to illustrate and explain the pulse compression effect. A mathematical proof was provided to confirm the understanding of this effect.

6.2 Significance of Work

This work represents the first time-domain analysis of the temporal response of a stable periodic structure with alternating layers of nonlinear materials with oppositely-signed Kerr coefficients.

Prior to this work there existed no systematic study of nonlinear solitonic and non-solitonic pulse behavior in such stable Bragg structures. As a result of this work, the questions outlined earlier in Chapter 2 have been fully addressed and the answers are summarized here:

- QUESTION: In what ways do the proposed nonlinear Bragg structure provide an improvement to optical signal processing over previously considered devices?

  ANSWER: The proposed nonlinear Bragg structure is complementary to the bistable optical switching devices such as nonlinear Fabry-Perot resonators. The structure was theoretically predicted to have the capability of achieving multiple optical signal processing functions including limiting (Sections 5.3 and 5.5), reshaping (Section 5.3), logic operations (Section 5.5), and pulse compression (Section 5.5).

- QUESTION: What are the important design issues in using nonlinear Bragg structures for practical optical signal processing?

  ANSWER: The device parameters and pulse properties were chosen according to the experimental literature for nonlinear materials properties (Section 4.4.1). The Kerr coefficients $n_{nl1,2}$ of the two adjacent layers were chosen to be $n_{nl1,2} = \pm 2.5 \times 10^{-12}$ cm^2/W, and the average linear index $(n_{01} + n_{02})/2$ was fixed at 1.50. The signal processing functions listed below used this range of parameters, as well as specifications for device length and incident pulse width.

  - Optical limiting may be achieved through the choice of the number of layers, peak intensity, and temporal width. For example, a pulse with FWHM = 605 fs was found to limit its transmitted peak intensity to 1.2, 1.6, and 2.8 GW/cm^2 for a 800-, 500-, and 180-layered device (i.e., 290, 180, and 70 μm), respectively.
  - An optical logic gate may be formed using a nonlinear periodic structure with a linear built-in grating. For example, a 0.01 out-of-phase linear grating (i.e., $n_{1,2} = (1.50 \mp 0.01) \pm 2.5 \times 10^{-12} I_{in}$) with a device length of at least 180 μm was shown to have S- and N-curve transfer characteristics. It had

  previously proven that such transfer characteristics allow a complete set of logic operations.

  - A pulse compressor may be designed by proper choice of the number of device layers and peak intensity. For example, a 720 μm-long device exhibited significant pulse compression, compressing a pulse down to 12% of its original width.

- QUESTION: How does the time-dependent (pulse-processing) behavior relate to the known steady-state responses?

  ANSWER: The limiting behavior and the S-curve transfer character are present in both the time-dependent and the steady-state response. The erasure and reopening of the stopband were shown to be responsible for these characteristics. However, in contradistinction with the steady-state average power results, the time-domain transmitted energy is not asymptotically limited. Temporal pulse compression makes the device attractive for signal processing. Section 5.5.2 investigated this special effect.

- QUESTION: What differentiates solitonic from non-solitonic propagation?

  ANSWER: A Bragg soliton propagates through a periodic structure in two coupled counter-propagating waves that maintain their shape; while a non-solitonic pulse propagates as a forward wave, then generates a reflected backward wave, and hence displays variations in pulse shape. In general, the strict requirements on peak power, initial pulse shape, and pulse duration needed to balance precisely the effects of dispersion and nonlinearity for producing a soliton may be difficult to satisfy. According to Chapters 3 and 4, the Bragg soliton that was induced in the structure (with $n_{1,2} = (1.50 \mp 0.01) \pm 2.5 \times 10^{-12} I_{in}$) was required to have a peak intensity of 55 GW/cm^2 and a narrow pulse width of ~27 fs. The Gaussian pulse used for the equivalent structure took a much lower peak intensity of 4 GW/cm^2 and a much wider pulse width of ∼605 fs.

6.3 Future Prospects

It is clear that in order to advance networks beyond the rate of electronics, there is a push to do more with optics and less with electronics in the core of the network. This work presented the theoretical analysis of a stable class of one-dimensional nonlinear periodic devices and predicted the design requirements for their time-domain processing functions. However, the model developed for this work does not include linear absorption, nor does it account for saturation of the nonlinearity. Furthermore, the time response of the nonlinear materials with Kerr coefficients on the order of 10^{-12} cm^2/W was assumed to be small relative to the widths of pulses considered. Following are a few future directions for the continuation of this work:

- Extend the physical model to account for absorption, saturation of the Kerr nonlinearity, and a material response time comparable to the pulse evolution time.
- Extend the theoretical work to two-dimensional devices to provide confinement in the lateral dimension.
- Further extend the numerical model to the consideration of three-dimensionally periodic devices. This corresponds to an implementation, currently being developed at the University of Toronto, of colloidal crystal-based self-organized photonic crystals whose constituent periodic repeat units consist of Kerr-nonlinear materials with nearly-matched linear refractive indices. The model would result in a series of coupled-mode equations which account for modes strongly coupled via vectors of the reciprocal photonic lattice.

Appendix A

Non-iterative Algorithm for Solving the CME System

The real functions u, v, w, and y satisfy the coupled system in Eq. (4.2) are:

$$\begin{aligned}\frac{\partial u}{\partial T}+\frac{\partial u}{\partial Z}+n_{0k}y+f(u,w,v,y)&=0,\\ -\frac{\partial w}{\partial T}-\frac{\partial w}{\partial Z}+n_{0k}v+f(w,u,y,v)&=0,\\ \frac{\partial v}{\partial T}-\frac{\partial v}{\partial Z}+n_{0k}w+f(v,y,u,w)&=0,\\ -\frac{\partial y}{\partial T}+\frac{\partial y}{\partial Z}+n_{0k}u+f(y,v,w,u)&=0.\end{aligned} \tag{A.1}$$

We use Crank-Nicholson finite difference method to solve the above partial differential equations. In Eq. (4.6), the derivatives of the functions u, v, w, and y are approximated. For example,

$$\frac{\partial u}{\partial T} = \frac{u^{\alpha}_{\beta+1}-u^{\alpha}_{\beta-1}}{2\Delta t}; \tag{A.2}$$

$$\frac{\partial u}{\partial Z} = \frac{1}{2}\left[\frac{\partial u^{\alpha}_{\beta+1}}{\partial Z}+\frac{\partial u^{\alpha}_{\beta-1}}{\partial Z}\right] = \frac{u^{\alpha+1}_{\beta+1}-u^{\alpha-1}_{\beta+1}}{4\Delta z}+\frac{u^{\alpha+1}_{\beta-1}-u^{\alpha-1}_{\beta-1}}{4\Delta z} \tag{A.3}$$

The element u^{α}_{β} represents the value of the function u at the grid point ($Z=\alpha\Delta z$, $T=\beta\Delta t$). This numerical method is known to be unconditionally stable for any values of Δt, Δz, and n_{0k} [11].

$$\begin{aligned}
&u^{\alpha}_{\beta+1} + \frac{\Delta t}{2\Delta z}(u^{\alpha+1}_{\beta+1} - u^{\alpha-1}_{\beta+1}) + (\Delta t n_{0k})y^{\alpha}_{\beta+1} \\
&\quad = u^{\alpha}_{\beta-1} - \frac{\Delta t}{2\Delta z}(u^{\alpha+1}_{\beta-1} - u^{\alpha-1}_{\beta-1}) - (\Delta t n_{0k})y^{\alpha}_{\beta-1} - 2\Delta t f^{\alpha}_{\beta}(u,w,v,y), \\
&w^{\alpha}_{\beta+1} + \frac{\Delta t}{2\Delta z}(w^{\alpha+1}_{\beta+1} - w^{\alpha-1}_{\beta+1}) + (\Delta t n_{0k})v^{\alpha}_{\beta+1} \\
&\quad = w^{\alpha}_{\beta-1} - \frac{\Delta t}{2\Delta z}(w^{\alpha+1}_{\beta-1} - w^{\alpha-1}_{\beta-1}) - (\Delta t n_{0k})v^{\alpha}_{\beta-1} - 2\Delta t f^{\alpha}_{\beta}(w,u,y,v), \\
&v^{\alpha}_{\beta+1} + \frac{\Delta t}{2\Delta z}(v^{\alpha+1}_{\beta+1} - v^{\alpha-1}_{\beta+1}) + (\Delta t n_{0k})w^{\alpha}_{\beta+1} \\
&\quad = v^{\alpha}_{\beta-1} - \frac{\Delta t}{2\Delta z}(v^{\alpha+1}_{\beta-1} - v^{\alpha-1}_{\beta-1}) - (\Delta t n_{0k})w^{\alpha}_{\beta-1} - 2\Delta t f^{\alpha}_{\beta}(v,y,u,w), \\
&y^{\alpha}_{\beta+1} + \frac{\Delta t}{2\Delta z}(y^{\alpha+1}_{\beta+1} - y^{\alpha-1}_{\beta+1}) + (\Delta t n_{0k})u^{\alpha}_{\beta+1} \\
&\quad = y^{\alpha}_{\beta-1} - \frac{\Delta t}{2\Delta z}(y^{\alpha+1}_{\beta-1} - y^{\alpha-1}_{\beta-1}) - (\Delta t n_{0k})u^{\alpha}_{\beta-1} - 2\Delta t f^{\alpha}_{\beta}(y,v,w,u).
\end{aligned} \tag{A.4}$$

The nonlinear function $f^{\alpha}_{\beta}(u,w,v,y)$ is defined by

$$\begin{aligned}
f^{\alpha}_{\beta}(u,w,v,y) = {} & n_{nl}[(u^{\alpha}_{\beta})^2 + (w^{\alpha}_{\beta})^2 + 2(v^{\alpha}_{\beta})^2 + 2(y^{\alpha}_{\beta})^2]w^{\alpha}_{\beta} \\
& + n_{2k}\{[(u^{\alpha}_{\beta})^2 + 3(w^{\alpha}_{\beta})^2 + (v^{\alpha}_{\beta})^2 + (y^{\alpha}_{\beta})^2]y^{\alpha}_{\beta} + 2u^{\alpha}_{\beta}w^{\alpha}_{\beta}v^{\alpha}_{\beta}y^{\alpha}_{\beta}\}
\end{aligned}$$

The system (A.4) can be used to evaluate functions of u^{α}_{β}, w^{α}_{β}, v^{α}_{β}, and y^{α}_{β} when $\alpha = 1, 2, \ldots, N$ and $\beta = 1, 2, \ldots, K$. The boundary values u^{0}_{β}, w^{0}_{β}, v^{0}_{β}, y^{0}_{β}, u^{N+1}_{β}, w^{N+1}_{β}, v^{N+1}_{β}, and y^{N+1}_{β} are considered separately. The boundary conditions in Eq. (4.8) state

$$\begin{aligned}
u^{0}_{\beta} = \sqrt{I_{in}(T)}, \qquad & w^{0}_{\beta} = \sqrt{I_{in}(T)}, \\
v^{N+1}_{\beta} = 0, \qquad & y^{N+1}_{\beta} = 0.
\end{aligned} \tag{A.5}$$

The three-point forward difference method is used for solving u, w, v, and y at the boundary $Z = 0$ and $z = L$.

$$\begin{aligned}
&u_{\beta+1}^{N+1} + \frac{\Delta t}{2\Delta z}(3u_{\beta+1}^{N+1} - 4u_{\beta+1}^{N} + u_{\beta+1}^{N-1}) \\
&\quad = u_{\beta-1}^{N+1} - \frac{\Delta t}{2\Delta z}(3u_{\beta-1}^{N+1} - 4u_{\beta-1}^{N} + u_{\beta-1}^{N-1}) - 2\Delta t f_{\beta}^{N+1}(u, w, v, y), \\
&w_{\beta+1}^{N+1} + \frac{\Delta t}{2\Delta z}(3w_{\beta+1}^{N+1} - 4w_{\beta+1}^{N} + w_{\beta+1}^{N-1}) \\
&\quad = w_{\beta-1}^{N+1} - \frac{\Delta t}{2\Delta z}(3w_{\beta-1}^{N-1} - 4w_{\beta-1}^{N} + w_{\beta-1}^{N-1}) + 2\Delta t f_{\beta}^{N+1}(w, u, y, v), \\
&v_{\beta+1}^{0} - \frac{\Delta t}{2\Delta z}(-v_{\beta+1}^{2} + 4v_{\beta+1}^{1} - 3v_{\beta-1}^{0}) = v_{\beta-1}^{0} \\
&\quad + \frac{\Delta t}{2\Delta z}(-v_{\beta-1}^{2} + 4v_{\beta-1}^{1} - 3v_{\beta-1}^{0}) - \Delta t n_{0k}(w_{\beta+1}^{0} + w_{\beta-1}^{0}) - 2\Delta t f_{\beta}^{0}(v, y, u, w), \\
&y_{\beta+1}^{0} - \frac{\Delta t}{2\Delta z}(-y_{\beta+1}^{2} + 4y_{\beta+1}^{1} - 3y_{\beta-1}^{0}) = y_{\beta-1}^{0} \\
&\quad + \frac{\Delta t}{2\Delta z}(-y_{\beta-1}^{2} + 4y_{\beta-1}^{1} - 3y_{\beta-1}^{0}) + \Delta t n_{0k}(u_{\beta+1}^{0} + u_{\beta-1}^{0}) + 2\Delta t f_{\beta}^{0}(y, v, w, u).
\end{aligned} \tag{A.6}$$

We thus obtain a non-iterative algorithm for solving the functions at a specific time instance:

$$\left\{\begin{aligned}
&\begin{bmatrix} A(\frac{\Delta t}{2\Delta z}) & C \\ -D & B(\frac{\Delta t}{2\Delta z}) \end{bmatrix} \begin{bmatrix} u_{\beta}^{\alpha+1} \\ y_{\beta}^{\alpha+1} \end{bmatrix} = \begin{bmatrix} A(-\frac{\Delta t}{2\Delta z}) & -C \\ D & B(-\frac{\Delta t}{2\Delta z}) \end{bmatrix} \begin{bmatrix} u_{\beta}^{\alpha-1} \\ y_{\beta}^{\alpha-1} \end{bmatrix} + \begin{bmatrix} H_{\beta}^{\alpha}(u, w, v, y) \\ H_{\beta}^{\alpha}(w, u, y, v) \end{bmatrix} \\
&\begin{bmatrix} A(\frac{\Delta t}{2\Delta z}) & -C \\ D & B(\frac{\Delta t}{2\Delta z}) \end{bmatrix} \begin{bmatrix} w_{\beta}^{\alpha+1} \\ v_{\beta}^{\alpha+1} \end{bmatrix} = \begin{bmatrix} A(-\frac{\Delta t}{2\Delta z}) & C \\ -D & B(-\frac{\Delta t}{2\Delta z}) \end{bmatrix} \begin{bmatrix} w_{\beta}^{\alpha-1} \\ v_{\beta}^{\alpha-1} \end{bmatrix} + \begin{bmatrix} H_{\beta}^{\alpha}(v, y, u, w) \\ H_{\beta}^{\alpha}(y, v, w, u) \end{bmatrix}
\end{aligned}\right. \tag{A.7}$$

where

$$A\left(\frac{\Delta t}{2\Delta z}\right) = \begin{bmatrix}
1 & \frac{\Delta t}{2\Delta z} & 0 & \cdots & 0 & 0 & 0 \\
-\frac{\Delta t}{2\Delta z} & 1 & \frac{\Delta t}{2\Delta z} & \cdots & 0 & 0 & 0 \\
0 & -\frac{\Delta t}{2\Delta z} & 1 & \cdots & 0 & 0 & 0 \\
\vdots & \vdots & \vdots & \cdots & \vdots & \vdots & \vdots \\
0 & 0 & 0 & \cdots & -\frac{\Delta t}{2\Delta z} & 1 & \frac{\Delta t}{2\Delta z} \\
0 & 0 & 0 & \cdots & \frac{\Delta t}{2\Delta z} & -4\frac{\Delta t}{2\Delta z} & 1 + 3\frac{\Delta t}{2\Delta z}
\end{bmatrix}, \tag{A.8}$$

$$B\left(\frac{\Delta t}{2\Delta z}\right) = \begin{bmatrix} 1+3\frac{\Delta t}{2\Delta z} & -4\frac{\Delta t}{2\Delta z} & \frac{\Delta t}{2\Delta z} & \cdots & 0 & 0 & 0 \\ \frac{\Delta t}{2\Delta z} & 1 & -\frac{\Delta t}{2\Delta z} & \cdots & 0 & 0 & 0 \\ 0 & \frac{\Delta t}{2\Delta z} & 1 & \cdots & 0 & 0 & 0 \\ \vdots & \vdots & \vdots & \cdots & \vdots & \vdots & \vdots \\ 0 & 0 & 0 & \cdots & \frac{\Delta t}{2\Delta z} & 1 & -\frac{\Delta t}{2\Delta z} \\ 0 & 0 & 0 & \cdots & 0 & \frac{\Delta t}{2\Delta z} & 1 \end{bmatrix}, \tag{A.9}$$

$$C = \Delta t n_{0k} \begin{bmatrix} 0 & 1 & 0 & \cdots & 0 & 0 & 0 \\ 0 & 0 & 1 & \cdots & 0 & 0 & 0 \\ \vdots & \vdots & \vdots & \cdots & \vdots & \vdots & \vdots \\ 0 & 0 & 0 & \cdots & 0 & 0 & 1 \\ 0 & 0 & 0 & \cdots & 0 & 0 & 0 \end{bmatrix}, \quad D = \Delta t n_{0k} \begin{bmatrix} 0 & 0 & 0 & \cdots & 0 & 0 & 0 \\ 1 & 0 & 0 & \cdots & 0 & 0 & 0 \\ \vdots & \vdots & \vdots & \cdots & \vdots & \vdots & \vdots \\ 0 & 0 & 0 & \cdots & 1 & 0 & 0 \\ 0 & 0 & 0 & \cdots & 0 & 1 & 0 \end{bmatrix} \tag{A.10}$$

And the matrices $H^{\alpha}_{\beta}(u,w,v,y)$, $H^{\alpha}_{\beta}(w,u,y,v)$, $H^{\alpha}_{\beta}(v,y,u,w)$, and $H^{\alpha}_{\beta}(y,v,w,u)$ are expressed as follows:

$$H^{\alpha}_{\beta}(u,w,v,y) = \\ -2\Delta t \begin{bmatrix} -\frac{\sqrt{I_{in}}}{2\Delta z} + f^0_0(u,w,v,y) & -\frac{\sqrt{I_{in}}}{2\Delta z} + f^0_1(u,w,v,y) & \cdots & -\frac{\sqrt{I_{in}}}{2\Delta z} + f^0_K(u,w,v,y) \\ f^1_0(u,w,v,y) & f^1_1(u,w,v,y) & \cdots & f^1_K(u,w,v,y) \\ \vdots & \vdots & \cdots & \vdots \\ f^N_0(u,w,v,y) & f^N_1(u,w,v,y) & \cdots & f^N_K(u,w,v,y) \\ f^{N+1}_0(u,w,v,y) & f^{N+1}_1(u,w,v,y) & \cdots & f^{N+1}_K(u,w,v,y) \end{bmatrix}, \tag{A.11}$$

$$H^{\alpha}_{\beta}(w,u,y,v) = 2\Delta t \begin{bmatrix} \sqrt{I_{in}}n_{0k} + f^0_0(w,u,y,v) & \sqrt{I_{in}}n_{0k} + f^0_1(w,u,y,v) & \cdots & \sqrt{I_{in}}n_{0k} + f^0_K(w,u,y,v) \\ f^1_0(w,u,y,v) & f^1_1(w,u,y,v) & \cdots & f^1_K(w,u,y,v) \\ \vdots & \vdots & \cdots & \vdots \\ f^N_0(w,u,y,v) & f^N_1(w,u,y,v) & \cdots & f^N_K(w,u,y,v) \\ f^{N+1}_0(w,u,y,v) & f^{N+1}_1(w,u,y,v) & \cdots & f^{N+1}_K(w,u,y,v) \end{bmatrix}, \tag{A.12}$$

$$H^{\alpha}_{\beta}(v,y,u,w) = 2\Delta t \begin{bmatrix} f^0_0(v,y,u,w) & f^0_1(v,y,u,w) & \cdots & f^0_K(v,y,u,w) \\ f^1_0(v,y,u,w) & f^1_1(v,y,u,w) & \cdots & f^1_K(v,y,u,w) \\ \vdots & \vdots & \cdots & \vdots \\ f^N_0(v,y,u,w) & f^N_1(v,y,u,w) & \cdots & f^N_K(v,y,u,w) \\ f^{N+1}_0(v,y,u,w) & f^{N+1}_1(v,y,u,w) & \cdots & f^{N+1}_K(v,y,u,w) \end{bmatrix}, \tag{A.13}$$

$$H^{\alpha}_{\beta}(y,v,w,u) = -2\Delta t \begin{bmatrix} f^0_0(y,v,w,u) & f^0_1(y,v,w,u) & \cdots & f^0_K(y,v,w,u) \\ f^1_0(y,v,w,u) & f^1_1(y,v,w,u) & \cdots & f^1_K(y,v,w,u) \\ \vdots & \vdots & \cdots & \vdots \\ f^N_0(y,v,w,u) & f^N_1(y,v,w,u) & \cdots & f^N_K(y,v,w,u) \\ f^{N+1}_0(y,v,w,u) & f^{N+1}_1(y,v,w,u) & \cdots & f^{N+1}_K(y,v,w,u) \end{bmatrix}. \tag{A.14}$$

The linear system described in Eq. (A.14) is implemented to calculate the values of u, v, w, y at the time instance $\beta\Delta t$.

Bibliography

[1] P. P. Mitra and J. B. Stark, “Nonlinear limits to the information capacity of optical fiber communications,” *Nature*, vol. 411, no. 6841, 2001.

[2] G. P. Agrawal, *Fiber-optic Communication Systems.* New York: Wiley, 1997.

[3] B. Mukherjee, *Optical Communicaiton Networks.* New York: McGraw-Hill, 1998.

[4] B. E. A. Saleh and M. C. Teich, *Fundamentals of Photonics.* New York: Wiley, 1991.

[5] P. W. E. Smith and W. J. Tomlinson, “Bistable optical devices promise subpicosecond switching,” *IEEE Spectr.*, vol. 8, no. 26, 1981.

[6] N. G. R. Broderick, D. Taverner, D. J. Richardson, M. Ibsen, and R. I. Laming, “Optical pulse compression in fiber Bragg gratings,” *Phys. Rev. Lett.*, vol. 79, no. 4566, 1997.

[7] N. G. R. Broderick, D. Taverner, D. J. Richardson, M. Ibsen, and R. I. Laming, “Experimental observation of nonlinear pulse compression in nonuniform Bragg gratings,” *Opt. Lett.*, vol. 22, no. 1837, 1997.

[8] C. J. Herbert, W. S. Capinsky, and M. S. Malcuit, “Optical power limiting with nonlinear periodic structures,” *Opt. Lett.*, vol. 17, no. 1037, 1992).

[9] L. Brzozowski and E. H. Sargent, “Nonlinear distributed-feedback structures as passive optical limiters,” *J. Opt. Soc. Am. B*, vol. 17, no. 1360, 2000.

[10] D. Pelinovsky, L. Brzozowski, J. Sears, and E. H. Sargent, "All-optical coherent signal processing realized with stable nonlinear periodic structure," *J. Opt. Soc. B*, vol. 19, no. 1, 2002.

[11] D. Pelinovsky and E. H. Sargent, "Stable all-optical limiting in nonlinear periodic structures. ii. computations," *J. Opt. Soc. B*, vol. 19, no. 8, 2002.

[12] W. N. Ye, L. Brzozowski, E. H. Sargent, and D. Pelinovsky, "Nonlinear propagation of ultrashort pulses in nonlinear periodic materials with oppositely-signed kerr coefficients," *LEOS 2001. 14th Annual Meeting of the IEEE Lasers and Electro-Optics Society*, vol. 2, no. 441, 2001.

[13] N. G. R. Broderick, D. Taverner, and D. J. Richardson, "Nonlinear switching in fiber Bragg gratings," *Opt. Express*, vol. 3, no. 11, 1998.

[14] L. Brzozowski and E. H. Sargent, "Optical signal processing using nonlinear distributed feedback structures," *IEEE J. Quantum Electron.*, vol. 36, no. 5, 2000.

[15] P. Yeh, *Optical Waves in Layered Media.* New York: Wiley, 1988.

[16] R. W. Boyd, *Nonlinear Optics.* London: Academic Press, 1992.

[17] C. M. de Sterke and J. E. Sipe, "Gap solitons," *Prog. in Optic.*, vol. 33, no. 203, 1994.

[18] B. J. Eggleton, R. E. Slusher, C. M. de Sterke, P. A. Krug, and J. E. Sipe, "Bragg grating solitons," *Phys. Rev. Lett.*, vol. 76, no. 10, 1996.

[19] W. Chen and D. L. Mills, "Gap solitons and the nonlinear optical response of superlattices," *Phys. Rev. Lett.*, vol. 58, no. 160, 1987.

[20] D. L. Mills and S. E. Trullinger, "Gap solitons in nonlinear periodic structures," *Phys. Rev. B*, vol. 36, no. 947, 1987.

[21] J. E. Sipe and H. G. Winful, “Nonlinear Schrödinger solitons in a periodic structure,” *Opt. Lett.*, vol. 13, no. 132, 1988.

[22] C. M. de Sterke and J. E. Sipe, “Envelope-function approach for the electrodynamics of nonlinear periodic structures,” *Phys. Rev. A*, vol. 38, no. 5149, 1988.

[23] D. N. Christodoulides and R. I. Joeseph, “Slow Bragg solitons in nonlinear periodic structures,” *Phys. Rev. Lett.*, vol. 62, no. 1746, 1989.

[24] A. B. Aceves and S. Wabnitz, “Self-induced transparency solitons in nonlinear refractive periodic media,” *Phys. Lett. A*, vol. 141, no. 37, 1989.

[25] N. D. Sankey, D. F. Prelewitz, and T. G. Brown, “All-optical switching in a nonlinear periodic-waveguide structure,” *Appl. Phys. Lett.*, vol. 60, no. 12, 1992.

[26] B. J. Eggleton, R. E. Slusher, C. M. de Sterke, P. A. Krug, and J. E. Sipe, “Modulational instability and tunable multiple soliton generation in apodized fiber gratings,” *Opt. Commun.*, vol. 149, no. 267, 1998.

[27] M. Scalora, J. P. Dowling, C. M. Bowden, and M. J. Bloemer, “Optical limiting and switching of ultrashort pulses in nonlinear photonic band gap materials,” *Phys. Rev. Lett.*, vol. 73, no. 10, 1994.

[28] Y. Lee, “Propagation dynamics of ultrashort optical pulses in nonlinear coupled-cavity-type multilayered structures: a numerical study,” *Opt. Rev.*, vol. 4, no. 20, 1997.

[29] N. S. Patel, K. L. Hall, and K. A. Rauschenbach, “Interferometric all-optical switches for ultrafast signal processing,” *Appl. Opt.*, vol. 37, no. 14, 1998.

[30] G. L. Wood, W. W. Clark, G. J. Salamo, and E. J. Sharp, “Evaluation of passive optical limiters and switches,” *Porc. SPIE*, vol. 1105, no. 154, 1989.

[31] E. Johnson and E. H. Sargent, “Function and sensitivity of signal processing systems using addition followed by limiting,” *J. Lightwave Technol.*, vol. 7, 2002.

[32] R. Rangel-Rojo, S. Yamada, H. Matsuda, and D. Yankelevich, “Large near-resonance third-order nonlinearity in an azobenzene functionalized polymer film,” *Appl. Phys. Lett.*, vol. 72, no. 9, 1998.

[33] H. S. Loka, S. D. Benjamin, and P. W. E. Smith, “Optical characterization of GaAs for ultrafast switching devices,” *IEEE Journal of Quantum Electron.*, vol. 34, no. 8, 1998.

[34] L. Qian, S. D. Benjamin, P. W. E. Smith, B. J. Robinson, and D. A. Thompson, “Picosecond carrier lifetime and large optical nonlinearities in InGaAsP grown by helium-plasma-assisted molecular beam epitaxy,” *Opt. Lett.*, vol. 22, no. 108, 1997.

[35] E. Garmire, “Resonant optical nonlinearities in semiconductors,” *IEEE J. Sel. Top. Quantum Electron.*, vol. 6, no. 6, 2000.

[36] A. Underhill, C. Hill, A. Charlton, S. Oliver, and S. Kreshaw, “Third-order NLO properties of PMMA films co-dispersed with metal Dithiolene oligomers,” *Synth. Met.*, vol. 71, no. 1703, 1995.

[37] L. Brzozowski and E. H. Sargent, “Azobenzenes for photonic network applications: Third-order nonlinear optical properties,” *J. Mater. Sci., Mater. Electron.*, vol. 12, no. 9, 2001.

[38] L. Brzozowski and E. H. Sargent, “All-optical analog-to-digital converters, hardlimiters, and logic gates,” *J. Lightwave Technol.*, vol. 15, no. 8, 2001.